Hydro-Mechanical-Seismological Modeling of Fluid-Induced Seismicity in Fractured Nonlinear Poroelastic Media: Theory, Implementation and Capabilities

Lei Jin[1*]

[1]Department of Geophysics, Stanford University, California 94305

*Corresponding to: Lei Jin (leijin@alumni.stanford.edu)

Key Points

- I consider an arbitrarily fractured, fluid-solid fully coupled and nonlinear poroelastic medium for modeling induced seismicity
- I propose a new framework coupling hydro-mechanical modeling with poroelastic stress path-based seismological modeling
- Three numerical experiments demonstrate model capabilities and effects of fractures and full coupling on overpressure, stress and seismicity

Abstract

Decoupled hydro-shearing has been a decades-long paradigmatic mechanism of fluid-induced seismicity. A surging alternative is coupled hydro-mechanical triggering, largely based on the theory of linear poroelasticity. Unfortunately, seismicity source fractures and their geometric and physical alterations to a canonical poroelastic system are rarely accounted for, and seismicity is typically forecasted using a Coulomb stress rate model without producing catalogs. Here, I present a new framework for modeling fluid-induced seismicity in arbitrarily fractured nonlinear poroelastic media. The hydro-mechanical triggering is modeled using our Jin & Zoback (2017, https://doi.org/10.1002/2017JB014892) computational model that resolves both fracture fluid storage and nonlinear flow in addition to full poroelastic coupling. Seismological modeling is achieved stochastically by generating stress drops based on the full inter-seismic poroelastic stressing history. The two steps are sequentially coupled and advanced in time via a new prediction-correction algorithm, allowing for fracture stress updating and synthetic event catalog assembly. To demonstrate model capabilities and effects of fractures and full coupling on overpressure, stress and seismicity, I perform three microseismic-scale numerical experiments by progressively adding fractures and poroelastic coupling into a diffusion-only base model. Some previously unknown mechanisms are elucidated. In contrast to existing models, my model produces repeaters and linear clustering of seismicity. Poroelastic coupling enhances the clustering, inhibits near-field seismicity over time while increasingly favoring remote triggering, and overall significantly reduces the event population. Meanwhile, some seismic source statistical characteristics including the Gutenberg-Richter scaling relation overall remain unaffected, and the curious *b*-value elevation for microseismicity can be attributed to a mechanical origin.

Keywords: coupled hydro-mechanical modeling, seismological modeling, induced seismicity, fractured porous media, poroelasticity, seismic source parameters

1. Introduction

Fluid perturbations (i.e., injection or withdrawal) within the subsurface alter the pore pressure and effective stress quasi-statically, inducing seismicity and dynamic stress release on certain fractures (in this study, I do not distinguish between a fracture and a fault, both defined as an arbitrarily long pre-existing permeable fluid pathway with frictional strength, and I shall use them inter-changeably). The occurrence of fluid-induced seismicity on a source fracture is due to the maximum shear stress resolved on it exceeds its static frictional strength. Adopting the classic linear Coulomb shear failure criterion, this can be summarized as

$$CFF = |\tau_f| - \mu_s \sigma'_{nf} = \left[\left\| \boldsymbol{\sigma}'_f \cdot \underline{n}_f \right\|^2 - \left(\boldsymbol{\sigma}'_f : \underline{n}_f \otimes \underline{n}_f \right)^2 \right]^{1/2} - \mu_s \left(\boldsymbol{\sigma}'_f : \underline{n}_f \otimes \underline{n}_f \right) \quad (1)$$

where $\boldsymbol{\sigma}'_f$ is the current effective stress tensor on the fracture in the presence of fluid perturbations, σ'_{nf}, $|\tau_f|$ and *CFF* are the effective normal stress, the maximum shear stress and the Coulomb Failure Function (i.e., Coulomb stress) resolved on the fracture, and $\underline{n}_f$ and μ_s are the unit normal vector and the static frictional coefficient of the fracture. Hereinafter the subscript f is used to indicate fracture-related quantities.

If fractures themselves are known *a priori*, i.e., $\underline{n}$ and μ_s are given, then the mechanics of fluid-induced seismicity fundamentally rests on the principle of effective stress (Dunham & Rice, 2008). For any given fluid-pressurized fracture, the current effective stress state can be decomposed as

$$\boldsymbol{\sigma}'_f = \boldsymbol{\sigma}'_{f0} + \delta\boldsymbol{\sigma}'_f \quad (2)$$

where $\boldsymbol{\sigma}'_{f0}$ is the arbitrary initial effective stress on the fracture and $\delta\boldsymbol{\sigma}'_f$ is the perturbation due to fluid overpressure within the fracture.

The key step in the hydro-shear process described by equation (1) then lies in the calculation of $\delta\boldsymbol{\sigma}'_f$. This is traditionally done in a fluid-solid decouple manner. Specifically, the mass conservation law in the form of fluid pressure diffusion is solved separately to obtain the overpressure within the fault, δp_f. The alteration to the fluid storage capacity due to solid deformation (i.e., the full volumetric strain for the fracture itself or a fraction of the volumetric strain for the fracture-hosting rock) is not accounted for. Following the Terzaghi simple effective stress law (Terzaghi, 1936), it is then assumed that the effective stress tensor is modified through isotropic reduction of all normal components by the amount of δp_f whereas all shear components remain unchanged. Following a compression positive notation, it can be summarized as

$$\delta\boldsymbol{\sigma}'_f = -\delta p_f \mathbf{1} = \begin{bmatrix} -\delta p_f & & \\ & -\delta p_f & \\ & & -\delta p_f \end{bmatrix} \tag{3}$$

Substituting equations (2) and (3) into equation (1), one recovers the familiar form of the Coulomb failure function with the pore pressure effect (e.g., Byerlee, 1978)

$$\begin{aligned} CFF &= \left[\left\| \boldsymbol{\sigma}'_{f0} \cdot \underline{n}_f \right\|^2 - \left(\boldsymbol{\sigma}'_{f0} : \underline{n}_f \otimes \underline{n}_f \right)^2 \right]^{1/2} - \mu_s \left(\boldsymbol{\sigma}'_{f0} : \underline{n}_f \otimes \underline{n}_f - \delta p_f \right) \\ &= |\tau_{f0}| - \mu_s \left(\sigma'_{nf0} - \delta p_f \right) \end{aligned} \tag{4}$$

where σ'_{nf0} and $|\tau_{f0}|$ are the initial effective normal stress and maximum shear stress on the fracture from $\boldsymbol{\sigma}'_{f0}$.

Equation (4) shows that the fluid overpressure within the fracture leads to a direct increase in its Coulomb stress (or effectively, a reduction in its static frictional strength) by the amount of $\mu_s \delta p_f$. To induce seismicity, i.e., the *CFF* is driven from negative to 0, the required δp_f is simply $(\sigma'_{nf0} - |\tau_{f0}|/\mu_s)$. This is widely used as a paradigm in designing experiments on fluid-induced seismicity both in the laboratory and on the field (e.g., Scuderi & Collettini, 2016; Mukuhira et al, 2017). This decoupled approach also remains as the basis of some prevalent statistical models of induced seismicity (e.g., Shapiro et al., 2005; Rothert & Shapiro, 2007). In this class of models, a statistically random critical pore pressure is used as a proxy of the frictional strength of a pre-existing fracture and the pore pressure evolution is governed by simple linear fluid diffusion; the modeled spatial-temporal distribution of seismicity, however, is often inconsistent with observations. As a remedy, some nonlinear diffusion models have been developed by adding a pressure-dependent diffusivity (Hummel & Shapiro, 2012; Johann et al., 2016; Carcione et al., 2018) in an attempt for better data matching. The diffusion-based seismicity models can be further extended by incorporating, e.g., random stress heterogeneity (Goertz-Allmann & Wiemer, 2012), fractures following distributions derived from field observations (Verdon et al., 2015), and even empirical seismic emission criteria for generating synthetic seismograms (Carcione et al., 2015). This decoupled mechanism also underlies some studies that invert for distributions of permeability (Tarrahi & Jafarpour, 2012) and pore pressure (Terakawa et al., 2012; Terakawa, 2014) from induced seismicity data.

Equation (4) also underlies some recent physics-based models for forecasting injection-induced seismicity. For example, the RSQSim earthquake simulator, originally developed in the absence of fluid flow and is aimed at improved modeling of seismicity through the inclusion of rate-and-state friction (Richards-Dinger & Dieterich, 2012), has been extended for forecasting induced seismicity by combining it with an analytical pressure diffusion model (Dieterich et al., 2015; Kroll et al., 2017). A model based on the so-called “seismogenic index”, which quantifies the seismotectonic state at an injection location

(Shapiro et al., 2010) and is locally calibratable using existing injection and seismicity data, has also been proposed and applied to seismicity forecasting at large scales (Langenbruch & Zoback, 2016; Langenbruch et al., 2018). The pressure rate used in the definition of the seismogenic index is derived from the standard pressure diffusion equation decoupled from solid stress state.

Despite their successful applications in many cases, the decoupled class of models has two fundamental drawbacks. First, they inherently cannot explain the remoting triggering of seismicity in areas not directly subjected to finite pressure perturbations (Stark & Davis, 1996; Megies & Wassermann, 2014; Yeck et al., 2016). They also incorrectly predict that pore pressure depletion increases the effective normal stress on a fault and therefore will always inhibit seismicity. However, depletion-induced faulting has been amply documented (e.g., Zoback & Zinke, 2002; Van Wees et al., 2014). The Biot theory of poroelasticity (Biot, 1941) provides a viable avenue to eliminating such dilemmas and subsume all observations under one paradigm. At its essence is the full monolithic coupling between the fluid and solid. Specifically, the negative pressure gradient acts an equivalent body force that enters the force balance law and drives changes in the solid deformation and stress; on the other hand, the volumetric strain rate acts an equivalent fluid source in the mass balance law and drives changes in the fluid overpressure (Segall, 2010; Jin & Zoback, 2017). Classic analytical solutions to a fully coupled linear poroelastic system under various simplifying conditions have been derived (e.g., Rice and Cleary, 1976; Cleary, 1977; Segall, 1985; Booker & Carter, 1986; Rudnicki, 1986; Segall & Fitzgerald, 1998; Wang & Kümpel, 2003). Pioneering studies have utilized this theory to explain depletion-induced seismicity (Segall, 1989; Segall et al., 1994) and more recently, probe its roles in injection-induced seismicity (Altmann et al., 2014; Segall & Lu, 2015). Since then the application of the theory of poroelasticity seems to have quickly arisen as a trend in establishing models of induced seismicity, and a rapidly growing body of studies have been documented recently, either analytically based (Jin & Zoback, 2015a; Dempsey & Suckale, 2017) or numerically based (e.g., Chang & Segall, 2016a; Chang & Segall, 2016b; Fan et al., 2016; Deng et al., 2016; Chang & Segall, 2017; Zbinden et al., 2017; Postma & Jansen, 2018; Tung & Masterlark, 2018; Chang & Yoon, 2018; Norbeck & Rubinstein, 2018). At a smaller scale, numerical simulations of fluid-induced microseismicity, typically motivated by applications like stimulations of hydrocarbon and geothermal reservoirs, have also been reported (e.g., Maillot et al., 1999; Angus et al., 2010; Baisch et al., 2010; Zhao & Young, 2011; Wassing et al., 2014; Yoon et al., 2014; Raziperchikolaee et al., 2014; Riffracture et al., 2016).

It is worth noting that a fully coupled poroelastic model has two important distinctions from a decoupled model. First, for the fluid, solid-to-fluid coupling can lead to non-monotonic solutions of the fluid pressure, due to changes in the pore (and fracture) volume caused by the compression or dilation of the solid skeleton. This was first observed in 2D by Mandel (1953) and later in 3D by Cryer (1963) and is collectively referred to as the *Mandel-Cryer effect*. Successfully replicating this phenomenon in the

numerical pressure solution is often considered as an important benchmark point (e.g., White & Borja, 2011). Second, for the solid, fluid-to-solid coupling generates a full and anisotropic poroelastic stress tensor instead of an isotropic stress tensor with only normal components as predicted by equation (3). Additionally, the magnitudes of the normal components differ from $-\delta p_f$. This has been documented in great details in Jin & Zoback (2017, 2018a, 2018b, 2019). In the context of induced seismicity, the second distinction is of our interest and it can be summarized as

$$\delta\boldsymbol{\sigma}'_f = \begin{bmatrix} \delta\sigma'_{fxx} & \delta\sigma'_{fxy} & \delta\sigma'_{fxz} \\ & \delta\sigma'_{fyy} & \delta\sigma'_{fyz} \\ symmetric & & \delta\sigma'_{fzz} \end{bmatrix} \tag{5}$$

Here, $\delta\sigma'_{fxx}$, $\delta\sigma'_{fyy}$, $\delta\sigma'_{fzz}$, $\delta\sigma'_{fxy}$, $\delta\sigma'_{fxz}$ and $\delta\sigma'_{fyz}$ are the six independent normal and shear components of $\delta\boldsymbol{\sigma}'_f$, which are to be solved for from the following quasi-static force balance law on the fault where the Terzaghi simple effective stress law applies (it is to be paired with the mass balance law in a monolithically coupled manner, details are not shown here, and the dependence of δp_f on the mean stress is indicated)

$$\begin{cases} \frac{\partial}{\partial x}\left(\delta\sigma'_{fxx}\right)+\frac{\partial}{\partial y}\left(\delta\sigma'_{fyx}\right)+\frac{\partial}{\partial z}\left(\delta\sigma'_{fzx}\right)+\frac{\partial}{\partial x}\left(\delta p_f\left(tr(\delta\boldsymbol{\sigma}'_f)\right)\right)=0 \\ \frac{\partial}{\partial x}\left(\delta\sigma'_{fxy}\right)+\frac{\partial}{\partial y}\left(\delta\sigma'_{fyy}\right)+\frac{\partial}{\partial z}\left(\delta\sigma'_{fzy}\right)+\frac{\partial}{\partial y}\left(\delta p_f\left(tr(\delta\boldsymbol{\sigma}'_f)\right)\right)=0 \\ \frac{\partial}{\partial x}\left(\delta\sigma'_{fxz}\right)+\frac{\partial}{\partial y}\left(\delta\sigma'_{fyz}\right)+\frac{\partial}{\partial z}\left(\delta\sigma'_{fzz}\right)+\frac{\partial}{\partial z}\left(\delta p_f\left(tr(\delta\boldsymbol{\sigma}'_f)\right)\right)=0 \end{cases} \tag{6}$$

Note that here the equilibrium needs to be sought only among the perturbating state itself since the arbitrary initial state is already in balance. In the coupled approach, the coulomb failure function equation (1) thus takes a more general form with the poroelastic effect

$$\begin{aligned} CFF &= \left[\left\|\left(\boldsymbol{\sigma}'_{f0}+\delta\boldsymbol{\sigma}'_f\right)\cdot\underline{n}_f\right\|^2-\left[\left(\boldsymbol{\sigma}'_{f0}+\delta\boldsymbol{\sigma}'_f\right):\underline{n}_f\otimes\underline{n}_f\right]^2\right]^{1/2}-\mu_s\left[\left(\boldsymbol{\sigma}'_{f0}+\delta\boldsymbol{\sigma}'_f\right):\underline{n}_f\otimes\underline{n}_f\right] \\ &= \left|\tau_{f0}+\delta\tau_f\right|-\mu_s\left(\sigma'_{nf0}+\delta\sigma'_{nf}\right) \end{aligned} \tag{7}$$

Comparing equation (7) with equation (4), the difference between the poroelastic effect and the pore pressure effect on seismicity triggering on a source fracture becomes clear. Generally speaking, $\delta\sigma'_{nf} \neq -\delta p_f$. The maximum shear stress on the fracture is also modified. The sense of $\delta\tau_f$ can be the same as or opposite to τ_{f0} and one must first sum up $\delta\boldsymbol{\sigma}'_f$ and $\boldsymbol{\sigma}'_{f0}$ before calculating the *CFF*. The distinction between equations (7) and (4) are vital as they can lead to radically different predictions on the time of rupture nucleation, the co-seismic rupture velocity, rupture style and radiation pattern as well as the post-seismic distributions of displacement and stress (Jin and Zoback, 2018a, 2018b).

While it has become increasingly recognized that the seismicity-triggering force within the fault-hosting rock is generated in a poroelastically coupled manner, there appear to be some unfortunate misconceptions. The first misconception is that pore pressure effect and poroelastic effect are alternative to each other and the former should be accepted as the correct approach when the Biot-Willis coefficient α of the hosting rock is less than 0.3 (Johann et al., 2016). The second misconception is that the pore pressure effect and the poroelatic effect co-exist such that induced seismicity is a result of both (e.g., Goebel et al., 2017; Barbour et al., 2017; Keranen & Weingarten, 2018; Skoumal et al., 2018; Yu et al, 2019). The reason why neither is valid becomes evident at this point. As has been shown above, the key difference between the pore pressure effect and the poroelastic effect in seismicity triggering lies in equations (3) and (6), which can now be summarized as

$$\delta\boldsymbol{\sigma}_f' + \delta p_f \mathbf{1} = \mathbf{0} \quad on\ \Omega_f \tag{8}$$

for pore pressure effect and

$$\nabla \cdot \left(\delta\boldsymbol{\sigma}_f' + \delta p_f \mathbf{1}\right) = \nabla \cdot \delta\boldsymbol{\sigma}_f' + \nabla \delta p_f = \underline{0} \quad on\ \Omega_f \tag{9}$$

for poroelastic effect.

Here $\mathbf{1}$ is the unit identity (Kronecker delta), $\mathbf{0}$ and $\underline{0}$ are a second-order tensor and a vector with all 0 constituents and Ω_f is the fracture domain. Equation (9) needs to be closed with appropriate boundary conditions. Obviously, the solution to equation (8) always satisfies equation (9); however, the solution to equation (9) does not always guarantee equation (8). In other words, equation (8) is sufficient but not necessary for equation (9). This is the case, for example, when δp_f is not spatially uniform (i.e., a gradient in δp_f is present, $\nabla \delta p_f \neq \underline{0}$). Under this condition, one can readily see that $\nabla \delta p_f$ acts as an equivalent body force vector and produces a full stress tensor. For the solution from equation (9) to be the same as that from equation (8), two simplifying conditions are needed. First, the pressure change δp_f is uniform such that

$$\nabla \delta p_f = \underline{0} \tag{10}$$

and second, the domain is subjected to zero incremental traction on the boundary, described by a Neumann type boundary condition

$$\left(\delta\boldsymbol{\sigma}_f' + \delta p_f \mathbf{1}\right) \cdot \underline{n}_f = \underline{0} \quad on\ \partial\Omega_f \tag{11}$$

where $\partial\Omega_f$ is the fracture domain boundary. Only under the conditions specified by equations (10) and (11) can the solution to equation (9) also satisfies equation (8). Therefore, I point out that the poroelastic effect (or more broadly speaking, the poromechanical effect in the presence of material nonlinearity like

plasticity and non-Darcy flow) is the true and only effect; the pore pressure effect is the "reduced" poroelastic effect under simplifying conditions and the two should not be considered as alternative nor co-existing effects.

For the fault-hosting porous rock itself, the degree of poroelastic coupling is scaled by the Biot coefficient α (typically below 1). Johann et al. (2016) hypothesize that for low-permeability rocks, α should also be negligible and they cast doubt on the validity of the Segall (2015, 2016a) poroelastic models in which α>0.3. This hypothesis is impertinent. α is a measurement of the rock solid's susceptibility to the influence of the fluid and vice versa. Its exact form was first rigorously derived from basic linear constitutive equations as (Nur & Byerlee, 1971)

$$\alpha = 1 - \frac{K_b}{K_m} \tag{12}$$

where K_b and K_m are the bulk moduli of the porous rock and the solid skeleton grains, respectively.

The exact same expression was later re-derived from the first and second laws of thermodynamics and it was shown that the Biot effective stress tensor arises naturally as power-conjugate to the rate of deformation tensor of the solid phase (Borja, 2006). Low permeability does not necessarily imply low porosity nor low α. The solid grains can be packed in a manner to maintain high porosity and low K_b (hence high α) with poor or little interconnections between pores (hence low permeability). As a matter of fact, laboratory experiments confirm that α of low-permeability shale reservoir rocks is indeed primarily between 0.3 and 0.9 (e.g., Hornby, 1995; He et al., 2016; Ma & Zoback, 2017). Returning to the first misconception discussed above, the conclusion by Johann et al. (2016) that the pore pressure effect can approximate the poroelastic effect when α<0.3 is merely a coincidence in the parameter space. It the case of a medium with overall low permeability, or with severe permeability contrasts (e.g., an ultra-low-permeability shale embedded with high-permeability fractures), the differences between distributions of pore pressure and poroelastic stress are drastic (Jin & Zoback, 2019).

The theory of poroelasticity is undoubtedly applicable to fluid-infiltrated and -saturated porous rock across a wide range of permeability scales. Classic analytical solutions offer important insights but are generally less applicable due to restricting conditions. Despite a surging number of numerical poroelastic models as have been mentioned above, applications of them to induced seismicity are rather limited. They are used to either analyze a single event or forecast seismicity rate based on the classic Dieterich Coulomb stress rate model (Dieterich, 1994), without modeling the spatial-temporal evolutions of seismicity nor their source and statistical characteristics. Notice also that these models either do not explicitly include faults or include very limited number of them and treat them simply as a porous domain with localized permeabilities, therefore the medium is effectively "porous" only. None offered the capacity to model geometrically complex fracture networks. More importantly, some first-order fracture-

related physics, for example, the Poiseuille flow behavior within the fracture and the associated nonlinearity due to pressure-induced hydraulic aperture variations, are not accounted for. Furthermore, limited within the capacity of commercial solvers, the fracture domain is often represented with exaggerated thickness (and therefore artificially enhanced along-fracture fluid flow) to facilitate equal-dimensional space discretization. These simplifications come with consequences and may diminish the meaningfulness of modeling outcomes (Jin & Zoback, 2016a, 2016b).

To date, a general mechanic-based and physically representative model of fluid-induced seismicity in a geologically realistic medium is not available, due to in part difficulties in establishing a suitable theoretical and computational framework for fluid-saturated, arbitrarily fractured and nonlinear poroelastic solid. As a result, effects of fractures and full coupling on triggering seismicity and controlling its evolutional and source characteristics also remain largely unexplored. We are therefore motivated to develop the following new hydro-mechanical-seismological modeling framework. Built upon our Jin & Zoback (2017) fracture-poro-mechanical computational model, this framework offers the capacity to handle arbitrarily distributed fractures and the associated new physics and nonlinearity. It also integrates for the first time deterministic modeling of inter-seismic, quasi-static and fluid-solid fully coupled triggering and mechanics-based stochastic modeling of co-seismic shear stress drop, and offers a natural way to model multiple induced seismic cycles. An important outcome of the modeling is a synthetic event catalog that allows for further statistical analysis. As a general tool, the model not only is capable of producing many phenomena observed in real data, but also allows for numerically uncovering some otherwise unknown effects of model configuration and physics on induced seismicity. Details are described below. Throughout the text, space- and time-dependent quantities in all equations are marked using ($\underline{x}$, t).

2. Theory and Implementation

2.1 Calculating Effective Stress on Fractures

As has been shown in section 1, the pivotal piece in modeling fluid induced seismicity lies in the calculation of the current effective stress tensor $\boldsymbol{\sigma}'_f$, defined on the fracture domain Ω_f. While it suffices to use Ω_f for describing the essence of poroelastic seismicity triggering (equations (2), (7) and (9)) and its fundamental difference from pore pressure triggering (equations (1), (2) and (8)), the calculation of $\boldsymbol{\sigma}'_f$ is a different issue. Directly solving equation (9) (coupled with a mass balance law) obviously requires discretizing an irregular stand-alone domain consists fractures with arbitrary locations and orientations as well as lengths and thicknesses that typically differ by orders of magnitude. Additionally, the fracture domain is coupled with the hosting rock through fluid and solid boundary conditions that are challenging to implement. One can circumvent this dilemma by indirectly solving for $\boldsymbol{\sigma}'_f$. To do so, the traction continuity condition across any given rock-fracture interface can be invoked,

$$\left[\overbrace{\boldsymbol{\sigma}(\underline{x},t)\cdot\underline{n}_f}^{hosting\,rock} - \overbrace{\underbrace{\left(\boldsymbol{\sigma}'_f(\underline{x},t)+p_f(\underline{x},t)\mathbf{1}\right)\cdot\underline{n}_f}_{\boldsymbol{\sigma}_f}}^{fracture} \right] = \underline{0} \quad \forall \underline{n}_f, \underline{x} \in \partial f \tag{13}$$

where $\boldsymbol{\sigma}$ and $\boldsymbol{\sigma}_f$ are the current Cauchy total stress tensor within the hosting rock (i.e., matrix) and on the fracture of interest, respectively, $\underline{n}_f$ and $\underline{0}$ are the same as before, and ∂f is the matrix-fracture interface.

Because equation (13) holds for any fracture of arbitrary orientation $\underline{n}_f$, it implies the following equality

$$\boldsymbol{\sigma}(\underline{x},t) - \boldsymbol{\sigma}_f(\underline{x},t) = \mathbf{0}, \ \underline{x} \in \partial f \tag{14}$$

Therefore, following the simple effective stress law, the effective stress tensor on the fracture of interest can be expressed as

$$\boldsymbol{\sigma}'_f(\underline{x},t) = \boldsymbol{\sigma}_f(\underline{x},t) - p_f(\underline{x},t)\mathbf{1} = \boldsymbol{\sigma}(\underline{x},t) - p_f\mathbf{1}(\underline{x},t), \ \underline{x} \in \partial f \tag{15}$$

To show the initial and perturbing states, equation (15) can be further expanded as

$$\boldsymbol{\sigma}'_f(\underline{x},t) = \left(\boldsymbol{\sigma}_0 + \delta\boldsymbol{\sigma}(\underline{x},t)\right) - \left(p_{f0} + \delta p_f(\underline{x},t)\right)\mathbf{1}, \ \underline{x} \in \partial f \tag{16}$$

where the subscript "0" indicates initial states whereas "δ" suggests perturbing states. Here, δp_f is the same as in equation (3) and is also referred to as the fluid overpressure within fractures or fault-zone overpressure.

2.2 Two Sources of Changes in Total Stress and Overpressure

From equation (16), it can be readily seen that the focus of the problem is now diverted towards solving for the two perturbing quantities: the Cauchy total stress tensor $\delta\boldsymbol{\sigma}$ in the poroelastic hosting rock and the fluid overpressure δp_f within fractures. Because the medium undergoes both fluid perturbations externally and seismicity internally, both variables can be decomposed to reflect these two sources as

$$\delta\boldsymbol{\sigma}(\underline{x},t) = \delta\boldsymbol{\sigma}_p(\underline{x},t) + \sum_j \delta\boldsymbol{\sigma}_s^{(j)}(\underline{x},t) H(CFF^{(j)}) \tag{17}$$

$$\delta p_f(\underline{x},t) = \delta p_{fp}(\underline{x},t) + \sum_j \underbrace{\delta p_{fs}^{(j)}(\underline{x},t)}_{\approx 0} H(CFF^{(j)}) \tag{18}$$

Here,

$$H(CFF) := \begin{cases} 0, & CFF < 0 \\ 1, & CFF \geq 0 \end{cases} \tag{19}$$

In equations (17), H is the Heaviside function, CFF is calculated according to equation (7), the subscript "p" indicates poroelastic changes arising from external fluid perturbations, the subscript "s" indicates seismicity-induced (i.e., fracture slip-induced) redistributions, and (j) refers to the number of episodes of slip on an event-generating source fracture. Here it is worth noting that external fluid perturbations fall into three categories: injection/withdraw pressure, surface flux (mass rate per unit area) and volume flux (mass rate per unit volume), the former two described by fluid Dirichlet and Neumann boundary conditions, respectively, and the last specified by a direct source/sink term. There appears to be some growing interest on which relates to induced seismicity the most (e.g., Barbour et al., 2017; Almakari et al., 2019; Alba et al., 2020; Hopp et al., 2020). Essentially, such differentiations are about testing the sensitivity of the governing law to the prescribed boundary conditions which all become parts of an external fluid mass vector for a linear problem and a residual vector for a nonlinear problem. Providing a universal answer should not be attempted, rather, the analysis ought to be done on a case-by-case basis.

Recall that mode-II slip on a source fracture yields negligible changes in the overpressure within it (volumetric strain occur in the hosting rock but not on the fracture), therefore, in this study, δp_{fs} is approximately 0 as is indicated in equation (18) such that $\delta p_f \approx \delta p_{fp}$ and can be solely attributed to external fluid perturbations.

Equations (17) and (18) must be substituted into equation (16) for determining if seismicity occurs on the fracture of interest according to equation (7); if yes, the seismic cycle needs to be updated ($j=j+1$) for this fracture. This process ought to be iterated over all time steps for all fractures. The major computational cost then arises from the calculation of external perturbations-induced changes $\delta\boldsymbol{\sigma}_p$ and δp_{fp} as well as seismicity-induced changes $\delta\boldsymbol{\sigma}_s$. The first two variables can be obtained from our Jin & Zoback (2017) computational model. The last variable can also be solved for in a fully dynamic spontaneous earthquake rupture problem with a loading history from the former two and this can be achieved using our Jin & Zoback (2018a, 2018b) computational model. For an arbitrarily fractured domain with a large fracture population, this task is perhaps computationally intractable. In this study, I seek intermediate solutions by focusing on the inter-seismic evolution of induced seismicity but not the co-seismic dynamic changes, therefore, rather than solving for all three for updating fracture stress, I will instead solve only for $\delta\boldsymbol{\sigma}_p$ and δp_{fp} and insert them into a novel fracture stress updating algorithm to indirectly account for the effect of $\delta\boldsymbol{\sigma}_s$ on source fractures without considering source-to-source interactions. The details of these two steps are given in the following three sections.

2.3 Fracture-Poro-Mechanical Modeling

2.3.1 Objective and Challenges

The objective of this section is to calculate $\delta\boldsymbol{\sigma}_p$ within the hosting rock and δp_{fp} within fractures as inputs for updating the Coulomb stress on fractures. Here, the total stress tensor $\delta\boldsymbol{\sigma}_p$ is further decomposed as the following according to the Biot effective stress law,

$$\delta\boldsymbol{\sigma}_p(\underline{x},t) = \delta\boldsymbol{\sigma}'_p(\underline{x},t) + \alpha\delta p_p(\underline{x},t)\mathbf{1} \tag{20}$$

where $\delta\boldsymbol{\sigma}'_p$ and δp_p are changes in the effective stress tensor and the fluid overpressure within the hosting rock due to external fluid perturbations, and α is the Biot-Willis coefficient.

Three major issues are posed here. First, from equations (16) and (20), it can now been seen that this step indeed involves three unknown variables, $\delta\boldsymbol{\sigma}'_p$, δp_p and δp_{fp}, and therefore requires solving three governing equations, including one force balance law for the hosting rock and two mass conservation laws for the hosting rock and fractures, respectively. This step is referred to as *fracture-poro-mechanical modeling*. Second, $\delta\boldsymbol{\sigma}'_p$ must be solved for simultaneously with the associated fluid overpressure δp_p in a fully coupled manner. Third, all three variables are functions of the arbitrary network of pre-existing fractures, which not only introduces additional fluid behaviors but also spans over a wide range of scales. While accounting for all fractures is probably computationally intractable, the subset of fractures at a scale comparable to the model domain must be deterministically resolved, as they have amply been demonstrated to have a first-order control of modeling outcomes (e.g., Berkowitz, 2002; Vujevic´ et al., 2014; Hirthe & Graf, 2015; Hardebol et al., 2015). I hereinafter refer to these fractures as the *large-scale deterministic fractures* (*LSDF*), which can be expressed as

$$LSDF = \bigcup_I^N F_I \tag{21}$$

where F_I *is the* I^{th} large-scale fracture and N is the total population.

2.3.2 Progressive Scenarios

To address the above issues and illustrate effects of the *LSDF* and full poroelastic coupling on seismicity, three progressive scenarios are constructed, each physically more representative than the previous. In the base scenario (case 1), I consider a fluid diffusion problem in a porous rock matrix Ω_m, which is governed by the following mass conservation law accompanied by the Darcy's flow equation. They read

$$\left(\phi_{m0}(\underline{x})\left(C_m + C_\rho\right)\right)\frac{\partial}{\partial t}\delta p_p(\underline{x},t) + \nabla\cdot\underline{v}(\underline{x},t) = s(\underline{x},t) \quad \underline{x}\in\Omega_m \tag{22}$$

$$\underline{v}(\underline{x},t) = -\eta^{-1}\mathbf{k}_m(\underline{x})\cdot\nabla\delta p_p(\underline{x},t) \quad \underline{x}\in\Omega_m \tag{23}$$

where ϕ_{m0} is the initial matrix porosity, C_m, C_ρ are compressibilities of the matrix and the fluid, respectively, $\underline{v}$ is the fluid velocity, s is the fluid source/sink term divided by the initial fluid density, η is the fluid viscosity, and $\mathbf{k}_\mathrm{m}$ is the full matrix permeability tensor permitted to be heterogeneous and fully anisotropic.

In the next scenario (case 2), I consider fluid diffusion in a fractured porous media by introducing the *LSDF* into the porous rock. In an equal-dimensional representation, the fractured domain is denoted as $\Omega=\Omega_m \cup \Omega_f$. For efficient computations without resolving transversal details across each fracture, Jin & Zoback (2017) proposed a new formulation customized for hydraulically conductive fractures. Due to its exceedingly thin nature, the fracture domain Ω_f can be reduced into a lower-dimensional domain superposed onto (instead of portioned from) the ambient matrix domain Ω_m such that $\Omega_f \subset \Omega_m = \overline{\Omega}$ where $\overline{\Omega}$ is a mixed-dimensional approximation of Ω. In this manner, fractures introduce no additional degrees of freedom (i.e., the unknown overpressure is now δp_p only rather than both δp_p and δp_{fp}), and the following relation holds

$$\delta p_{fp} \subset \delta p_p \tag{24}$$

However, the fluid storage capacity of the medium is now augmented due to the presence of fractures and the mass balance over the fractured domain now reads (Jin & Zoback, 2017)

$$\left(\Lambda_0(\underline{x})\phi_{m0}(\underline{x})\left(C_m + C_\rho\right) + \left(1-\Lambda_0(\underline{x})\right)\left(C_f + C_\rho\right)\right)\frac{\partial}{\partial t}\delta p_p(\underline{x},t) + \nabla \cdot \underline{v}(\underline{x},t) = s(\underline{x},t) \qquad \underline{x} \in \overline{\Omega} \tag{25}$$

where Λ_0 is a locally defined geometric factor that depends on the initial hydraulic aperture of fractures and C_f is the fracture compressibility.

Also, the hydraulic conductivity of the medium is enhanced and the addition of a nonlinear Poiseuille flow equation is needed for describing the localized fluid behavior within fractures. It reads

$$\underline{v}(\underline{x},t) = -\eta^{-1}\frac{1}{12}\left(b_0\left(1+C_f\delta p_{fp}(\underline{x},t)\right)\right)^2 \nabla_\tau \delta p_{fp}(\underline{x},t) \qquad \underline{x} \in \Omega_f \tag{26}$$

where b_0 is the initial hydraulic aperture of fractures and ∇_τ is the tangential gradient operator.

Poroelasticity is not considered in scenarios 1 and 2. In the last scenario (case 3), I further introduce full poroelastic coupling to the mixed-dimensional fractured domain $\overline{\Omega}$. The mass conservation law shown by equation (25) now needs a further modification to reflect a second change to the fluid storage capacity due to the solid matrix volumetric strain. Following a compression positive notation, it reads (Jin & Zoback, 2017)

$$\begin{aligned}&\left(\Lambda_0(\underline{x})\phi_{m0}(\underline{x})\left(C_m+C_\rho\right)+\left(1-\Lambda_0(\underline{x})\right)\phi_{f0}(\underline{x})\left(C_f+C_\rho\right)\right)\frac{\partial}{\partial t}\delta p_p(\underline{x},t)\\&-\alpha\nabla\cdot\left(\frac{\partial}{\partial t}\delta\underline{u}_p(\underline{x},t)\right)+\nabla\cdot\underline{v}(\underline{x},t)=s(\underline{x},t)\qquad \underline{x}\in\bar{\Omega}\end{aligned}\tag{27}$$

Equation (27) is to be fully and monolithically coupled with the following quasi-static force balance law

$$\nabla\cdot\left(\delta\boldsymbol{\sigma}'_p(\underline{x},t)+\alpha\delta p_p(\underline{x},t)\mathbf{1}\right)=\nabla\cdot\delta\boldsymbol{\sigma}'_p(\underline{x},t)+\alpha\nabla\delta p_p(\underline{x},t)=\underline{0}\qquad \underline{x}\in\bar{\Omega}\tag{28}$$

In this study, I consider the fractured medium in its entirety as linear elastic and adopt the Hooke's law

$$\delta\boldsymbol{\sigma}'_p(\underline{x},t)=\mathbf{D}:\nabla^{(s)}\delta\underline{u}_p(\underline{x},t)\qquad \underline{x}\in\bar{\Omega}\tag{29}$$

Here in equations (27) and (29), $\delta\underline{u}_p$ is the change to the solid matrix displacement vector due to external fluid perturbations, $\mathbf{D}$ is the elastic stiffness tensor, $\nabla^{(s)}$ is the symmetric gradient operator and ":" indicates double tensor contraction.

Table 1 summarizes the three progress scenarios, the latter two being nonlinear. The nonlinearity is sourced from equation (26) and is two-fold, as is manifested by first the pressure-dependent hydraulic aperture and second, the fracture permeability as a quadratic function of the hydraulic aperture, therefore the medium becomes nonlinearly poroelastic. Such form of nonlinearity is typically not included in previous seismicity modeling studies.

Table 1. Three progressive scenarios

Scenarios	**Governing equations**				**Descriptions**
	Fluid		*Solid*		
	Conservation	Flow	Balance	Constitutive	
Case 1	(22)	(23)	N/A	N/A	Fluid diffusion in a porous medium; linear
Case 2	(25)	(23), (26)	N/A	N/A	Fluid diffusion in a fractured porous medium; nonlinear
Case 3	(27)	(23), (26)	(28)	(29)	Fully monolithically coupled fluid diffusion and solid stressing in a fractured poroelastic medium; nonlinear

In seeking for a numerical solution, Jin & Zoback (2017) developed a hybrid-dimensional two-field mixed finite element method for efficient space discretization while preserving the distribution of a given set of deterministic fractures; the solution of the fully coupled semi-discrete system is advanced in time in a fully coupled manner (as opposed to a sequentially coupled manner) following a fully implicit (backward Euler) finite difference scheme; within each time step, the resulting nonlinear and fully discrete equation is solved using a Newton-Raphson solver. This technique is adopted for case 3. For case 1, the discretization is done in space using a standard Galerkin finite element method and in time using a backward Euler scheme; no linearization is needed. For case 2, the discretization and linearization procedures resemble those in case 3 except for the use of a single-field interpolation scheme. To illustrate the differences, for cases 1-3, I give their respective semi-discrete forms of the governing laws shown in table 1 after space discretization. They read

$$\tilde{\mathbf{M}}\dot{\hat{\zeta}}_p + \mathbf{K}\hat{\zeta}_p - \underline{F}_1 = \underline{0} \tag{30}$$

$$\left(\mathbf{M} + \sum_{I}^{N}\mathbf{M}_{F_I}(\hat{\zeta}_{pF_I})\right)\dot{\hat{\zeta}}_p + \left(\mathbf{K} + \sum_{I}^{N}\mathbf{K}_{F_I}(\hat{\zeta}_{pF_I})\right)\hat{\zeta}_p - \underline{F}_2 = \underline{R}_2 \tag{31}$$

$$\begin{bmatrix} \mathbf{M} + \sum_{I}^{N}\mathbf{M}_{F_I}(\hat{\zeta}_{pF_I}) & -\mathbf{C}^T \\ \mathbf{0} & \mathbf{0} \end{bmatrix}\begin{Bmatrix} \dot{\hat{\zeta}}_p \\ \dot{\underline{d}}_p \end{Bmatrix} + \begin{bmatrix} \mathbf{K} + \sum_{I}^{N}\mathbf{K}_{F_I}(\hat{\zeta}_{pF_I}) & \mathbf{0} \\ \mathbf{C} & \mathbf{G} \end{bmatrix}\begin{Bmatrix} \hat{\zeta}_p \\ \underline{d}_p \end{Bmatrix} - \begin{Bmatrix} \underline{F}_3 \\ \underline{Y} \end{Bmatrix} = \underline{R}_3 \tag{32}$$

where $\tilde{\mathbf{M}}$ and $\mathbf{M}$ are fluid storage capacity matrices in the absence and presence of fractures, respectively, $\mathbf{K}$ is the hydraulic conductivity/transferability matrix, $\mathbf{G}$ is the stiffness matrix, $\mathbf{C}$ is the coupling matrix, $\underline{F}_1$, $\underline{F}_2$ and $\underline{F}_3$, which take different forms, are external nodal mass vectors for cases 1-3, $\underline{Y}$ is the external nodal force vector, $\hat{\zeta}_p$ and $\underline{d}_p$ are nodal values of δp and $\delta\underline{u}_p$, respectively, augmenting quantities associated the *LSDF* are indicated with the subscript "F_I" and I and N are the same as in equation (21). The detailed expressions of the above discrete matrices and vectors can be found in Jin & Zoback (2017). $\tilde{\mathbf{M}}$, $\underline{F}_1$, $\underline{F}_2$ can be obtained by removing the fracture effect and/or the coupling effect from their respective counterparts.

Solving the fully discrete form of equations (30) - (32) gives their respective final numerical solutions. For the two cases with fractures (cases 2 and 3), the numerical solution of fracture overpressure δp_{fp}, denoted as $\hat{\zeta}_{fp}$, is then obtained by extracting a subset of the hosting rock pressure nodal values,

$$\hat{\zeta}_{fp} = \mathbf{Q}\hat{\zeta}_p \tag{33}$$

where $\mathbf{Q}$ is a matrix with 0 and 1 constituents. Details can be found on Jin and Zoback (2017).

Additionally, for case 3, the numerical solution of $\delta\boldsymbol{\sigma}'_p$ is in the so-called Voigt notation and it is calculated from $\underline{d}_p$ as

$$\delta\boldsymbol{\sigma}'_p = \mathbf{DB}\underline{d}_p \tag{34}$$

where $\mathbf{B}$ is standard finite element displacement-strain transformation matrix (e.g., Hughes, 2012).

2.3.3 Poroelastic Stress Invariants

In the fully coupled scenario (case 3), to examine and understand roles of poroelastic stressing in seismicity evolution, the distribution of *CFF* within the hosting rock is often plotted. In the presence of several faults with the same orientations, this step is straightforward (e.g., Chang & Segall, 2016a). In the case with varying fracture orientations, however, it is pragmatic to define an equivalent *CFF* calculated

from stress invariants. Here, two poroelastic stress invariants are calculated according to standard formulations except for the use of the effective poroelatic stress tensor $\delta\boldsymbol{\sigma}'_p$. Under plane strain, they read:

$$\frac{1}{3}I_1' = \frac{1}{3}(1+\nu)\left(\delta\sigma'_{px}+\delta\sigma'_{py}\right) \tag{35}$$

$$\sqrt{J_2'} = \sqrt{\frac{1}{6}\left[\left(\delta\sigma'_{px}-\delta\sigma'_{py}\right)^2+\left(\delta\sigma'_{py}-\nu\left(\delta\sigma'_{px}+\delta\sigma'_{py}\right)\right)^2+\left(\delta\sigma'_{px}-\nu\left(\delta\sigma'_{px}+\delta\sigma'_{py}\right)\right)^2\right]+\left(\delta\sigma'_{pxy}\right)^2} \tag{36}$$

where ν is the Poisson's ratio, $\delta\sigma'_{px}$, $\delta\sigma'_{py}$ are the two normal components and $\delta\sigma'_{pxy}$ is the shear component of $\delta\boldsymbol{\sigma}_p$', I_1' and $\sqrt{J_2'}$ are the first and second poroelastic stress invariants.

Using these two invariants, an *excess poroelastic shear stress* denoted as *MC*, is defined,

$$MC = \sqrt{J_2'} - \sin(\phi)\frac{1}{3}I_1' \tag{37}$$

Here,

$$\phi = \tan^{-1}(\mu_s) \tag{38}$$

Equation (37) is adapted from the invariant form of the Mohr Coulomb yield function (e.g., Borja, 2013) by setting the cohesion to 0 and the Lode's angle as π/6. In a sense, *MC* is the invariant form of *CFF*.

2.4 Inputs Preparation

At this point, for the two scenarios with fractures (cases 2 and 3), equation (16) can now be elaborated as the following

$$\boldsymbol{\sigma}'_f(\underline{x},t) = \left(\boldsymbol{\sigma}_0 + \delta\boldsymbol{\sigma}_p(\underline{x},t) + \sum_j \delta\boldsymbol{\sigma}_s^j(\underline{x},t)H(CFF^j)\right) - \left(p_{f0} + \overbrace{\delta p_{fp}(\underline{x},t) + \sum_j \underbrace{\delta p_{fs}^j(\underline{x},t)}_{\approx 0} H(CFF^j)}^{\delta p_f(\underline{x},t),\ \approx \delta p_{fp}(\underline{x},t)}\right)\mathbf{1} \quad \underline{x} \in \partial f \tag{39}$$

Applying the simple effective stress law for fractures, equation (39) collapses into a more general form

$$\boldsymbol{\sigma}'_f(\underline{x},t) = \boldsymbol{\sigma}'_{f0} + \delta\boldsymbol{\sigma}'_{fp}(\underline{x},t) + \sum_j \delta\boldsymbol{\sigma}'^j_{fs}(\underline{x},t)H(CFF^j) \tag{40}$$

where $\delta\boldsymbol{\sigma}'_{fp}=\delta\boldsymbol{\sigma}_p-\delta p_{fp}\mathbf{1}$ and $\delta\boldsymbol{\sigma}'_{fs}=\delta\boldsymbol{\sigma}_s-\delta p_{fs}\mathbf{1}$ are the effective stress changes on fractures from external fluid perturbations and seismicity, respectively, and their summation is $\delta\boldsymbol{\sigma}'_f$ shown in equation (2). Also, $\delta\boldsymbol{\sigma}'_{fs}\approx\delta\boldsymbol{\sigma}_{fs}$.

Here, the numerical solution of $\delta\boldsymbol{\sigma}'_{fp}$ vary among scenarios and its expression is obtained from equations (3) and (33) for case 2 and equations (20), (34) for case 3. For case 1, since fractures are absent, the definition of fracture effective stress does not apply. Nevertheless, to facilitate seismicity modeling, pre-defined random critical pore pressure as described in Shapiro et al. (2005) can be seeded in the domain, and an equivalent $\delta\boldsymbol{\sigma}'_{fp}$ (which indeed should be written as $\delta\boldsymbol{\sigma}'_{p}$), can be defined similar to equation (3). In mixed finite element discretization, numerical solutions reside at nodes for the fluid pressure but integration points for the stress. The mixed-field elements in Jin & Zoback (2017) are equal-lower-order, leading to element-wise constant strain and stress. Accordingly, to compute the element-wise effective stress, the element-averaged nodal fluid pressure is used. Mapped back into the tensor notation, the above is summarized as

$$\delta\boldsymbol{\sigma}'_{fp} = \begin{cases} -\alpha\left(\hat{\zeta}_p\right)_{mean}\mathbf{1}, & case\,1 \\ -\left(\mathbf{Q}\hat{\zeta}_p\right)_{mean}\mathbf{1}, & case\,2 \\ \left(\mathbf{DB}\underline{d}_p\right)_{Voigt\rightarrow tensor} + \alpha\left(\hat{\zeta}_p\right)_{mean}\mathbf{1} - \left(\mathbf{Q}\hat{\zeta}_p\right)_{mean}\mathbf{1}, & case\,3 \end{cases} \tag{41}$$

2.5 Seismological Modeling

The modeling outcomes from section 2.3 provide essential inputs for seismicity modeling. The remaining task here is to iteratively determine if seismicity occurs from equation (7), and if yes, update the stress on fractures and generate a synthetic event catalog.

2.5.1 A Dual-Scale Discrete Fracture Network

A dual network of fractures, hereinafter referred to as the *DF*, is considered as the source for seismicity. It consists of two complementary subsets A and B, where the subset A, denoted as $\widetilde{LSDF}$, is an approximation to the *LSDF* using a series of discrete fractures and the subset B is a stochastic representation of small-scale fractures typically found in the surrounding hosting rock and is hereinafter referred to as the *SSSF*. The above description can be summarized as:

$$DF = LSDF \cup SSSF = \left(\bigcup_a^{n_A} f_a\right) \cup \left(\bigcup_b^{n_B} f_b\right) \tag{42}$$

where f_a is the a^{th} fracture in the subset A, f_b is the b^{th} fracture in the subset B, and n_a and n_b are the respective populations.

2.5.2 Stochastic Stress Drop Modeling Constrained by Poroelastic Stressing History

As has been discussed in section 2.2, fracture stress will be updated first using external perturbation-induced changes and then corrected to account for slip-induced redistributions. To this end, two simplifications are made. First, source-to-source interactions are neglected, i.e., stress on a fracture is not

affected by slip on nearby fractures. Second, slip causes negligible changes in the effective normal stress on the source fracture itself. This reads

$$\delta\boldsymbol{\sigma}'_{fs}(\underline{x},t):\underline{n}_f\otimes\underline{n}_f\approx 0 \tag{43}$$

Combined with equation (40), equation (43) implies that

$$\boldsymbol{\sigma}'_f(\underline{x},t):\underline{n}_f\otimes\underline{n}_f\approx\left(\boldsymbol{\sigma}'_{f0}(\underline{x})+\delta\boldsymbol{\sigma}'_{fp}(\underline{x},t)\right):\underline{n}_f\otimes\underline{n}_f \tag{44}$$

Therefore the shear stress on the fracture after slip can now be re-written in the following form

$$\sqrt{\left\|\boldsymbol{\sigma}'_f(\underline{x},t)\cdot\underline{n}_f\right\|^2-\left(\boldsymbol{\sigma}'_f(\underline{x},t):\underline{n}_f\otimes\underline{n}_f\right)^2}=\sqrt{\left\|\left(\boldsymbol{\sigma}'_{f0}+\delta\boldsymbol{\sigma}'_{fp}(\underline{x},t)\right)\cdot\underline{n}_f\right\|^2-\left(\left(\boldsymbol{\sigma}'_{f0}+\delta\boldsymbol{\sigma}'_{fp}(\underline{x},t)\right):\underline{n}_f\otimes\underline{n}_f\right)^2}-\sum_j\Delta\tau_j \tag{45}$$

Here, $\Delta\tau_j$ is the static shear stress drop on the fracture due to the j^{th} episode of slip. The constrained stochastic stress drop modeling on a source fracture based on its full poroelastic loading history is describe by

$$\Delta\tau_j=r\Delta\tau_{j\max} \tag{46}$$

Here,

$$\Delta\tau_{j\max}=(\mu_s-\mu_d)\left(\boldsymbol{\sigma}'_{f0}+\delta\boldsymbol{\sigma}'_{fp}(\underline{x},t_j^*)\right):\underline{n}_f\otimes\underline{n}_f \tag{47}$$

In equations (46) and (47), t_j^* is the time at which the j^{th} episode of slip occurs, μ_d is the fracture dynamic frictional coefficient as is typically used in a slip-weakening law (Andrews, 1976), $\Delta\tau_{j\max}$ is the maximum likely shear stress drop and r is a stochastic parameter between 0 and 1 in honor of potential non-full degree of stress drop (see also Verdon et al., 2015). The distribution of $\Delta\tau_j$ is a convolution of distributions of r and $\Delta\tau_{jmax}$. In this study, since $\Delta\tau_{jmax}$ is deterministically modeled, only the distribution of r is needed, which is assumed to be uniform on [0, 1]. Equations (46) and (47) state that first, the new shear stress on a fracture due to seismicity is constrained above a lower bound defined by the residual frictional strength of the fracture and second, the maximum likely shear stress drop on a source fracture is determined by its full inter-seismic poroelastic loading history. This is an improvement on directly prescribing the shear stress drop in previous studies (e.g., Izadi & Elsworth, 2014).

2.5.3 Source Parameter Calculations

The key equations used in calculating the seismic source parameters are shown here. First, the seismic moment M_0 can be calculated from the fracture dimension and the recorded $\Delta\tau$. Depending on the fracture geometry and the faulting regime, various formulas are available. Here, I opt for the one suitable for a rectangular dip-slip fracture (Kanamori and Anderson, 1975):

$$M_0 = \frac{\pi(\lambda + 2\mu)}{4(\lambda + \mu)} \Delta\tau W^2 L \tag{48}$$

where W is the fracture width (assumed as 1 m in numerical examples under plane strain), λ and μ are the Lame's constant and the shear modulus of the medium.

Second, the moment magnitude M_w is calculated from M_0 following (Hanks & Boore, 1984):

$$Mw = \frac{2}{3}(\lg M_0 - 9.1) \tag{49}$$

2.5.4 Fracture Stress Updating Algorithm

Inspired by the prediction-correction type of algorithm in plasticity computational modeling, here I propose the following incremental fracture stress updating and seismicity generation algorithm. The overshoot in the inter-seismic prediction step can be minimized by reducing the time step used for matching the solutions of equations (30) - (32).

List 1. Incremental fracture stress updating algorithm

for fracture f_i % within the *DF*, equation (42)
  for time step t_k
    get $\boldsymbol{\sigma}'_{fp}(f_i,t_k)$, $\boldsymbol{\sigma}'_{fp}(f_i,t_{k-1})$ % calculated and stored in sections 2.3 and 2.4
    get $\sigma'_{fn}(f_i,t_{k-1})$, $\tau_f(f_i,t_{k-1})$, $CFF(f_i,t_{k-1})$ from t_{k-1}
    predict $\tilde{\sigma}'_{fn}(f_i,t_k)$, $\tilde{\tau}_f(f_i,t_k)$, $\tilde{C}FF(f_i,t_k)$ from $\boldsymbol{\sigma}'_f(f_i,t_k) = \boldsymbol{\sigma}'_{f0}(f_i) + \delta\boldsymbol{\sigma}'_{fp}(f_i,t_k)$ % equation (7)
    % incremental poroelastic stress compensation on the fracture (inter-seismic)

$$\sigma'_{fn}(f_i,t_k) = \sigma'_{fn}(f_i,t_{k-1}) + \left(\tilde{\sigma}'_{fn}(f_i,t_k) - \sigma'_{fn}(f_i,t_{k-1})\right)$$

$$\tau_f(f_i,t_k) = \tau_f(f_i,t_{k-1}) + \left(\tilde{\tau}_f(f_i,t_k) - \tau_f(f_i,t_{k-1})\right)$$

$$CFF(f_i,t_k) = CFF(f_i,t_{k-1}) + \left(\tilde{C}FF(f_i,t_k) - CFF(f_i,t_{k-1})\right)$$

    % correction for seismicity-induced shear stress drop on the fracture, if any (co-seismic)
      if $CFF(f_i,t_k) \geq 0$

$$\Delta\tau(f_i,t_k) = r(\mu_s - \mu_d)\sigma'_{fn}(f_i,t_k)$$ % equations (46), (47)

$$\tau_f(f_i,t_k) = \mu_s\sigma'_{fn}(f_i,t_k) - \Delta\tau(f_i,t_k)$$ % update the fracture shear stress

$$CFF(f_i,t_k) = \tau_f(f_i,t_k) - \mu_s\sigma'_{fn}(f_i,t_k) = -\Delta\tau(f_i,t_k)$$ % update the fracture *CFF*

        nos=nos+1 % number of seismic cycles
        record and calculate seismic source parameters % section 2.5.3
      end
  end
end

In list 1, the fracture f_i needs to be associated with a stress tensor $\delta\boldsymbol{\sigma}'_{fp}(f_i, t)$. Since f_i can intersect multiple elements (or Gauss integration points if using high-order finite elements), here, I will use only the stress tensor from the element nearest to its center. The above algorithm automatically produces multiple seismic cycles and therefore offers a natural way of modeling repeating events. I am now at a place to

proceed to the seismological modeling, see figure 1 for a schematic illustration. A complete seismicity catalog containing information on, e.g., the event origin time t_0, the location $\underline{x}$, the shear stress drop $\Delta\tau$, the seismic moment M_0, the moment magnitude M_w, the fracture length L and the initial Coulomb stress CFF_0, can be assembled. Notice in equation (48), a unit length along the third dimension is used. Additionally, the definitions of a triggered event and an induced event are given and they will be elaborated later in section 4.3.3 and used there for classifying the modeled events.

3. Microseismic-Scale Numerical Example Model Set-Up

3.1 Step 1 for Fracture-Poro-Mechanical Modeling

As a microseismic-scale numerical example, a 200 m × 200 m 2D domain is constructed representing a fracture-hosting porous rock. For cases 2 and 3, a *LSDF* with 100 constituents with lengths ranging from 20 m to 50 m, and orientations, from 0 to 360°, is resolved, see figure 2a. The model domain is then discretized in space, see figure 2b, to arrive at the semi-discrete forms given by equations (31) and (32). For case 1, no fracture is present; nevertheless, for meaningful comparisons, the same mesh is used for arriving at equation (30). For cases 2 and 3, the nominal model parameters, including the hydraulic and mechanical properties, the coupling coefficient of the hosting rock (i.e., the Biot-Willis coefficient α), the fluid and solid boundary conditions and the time-stepping parameter are identical to those in Jin & Zoback (2017). A particular quantity of interest is the hydraulic diffusivity of the hosting rock and the *LSDF* in cases 2 and 3, which are 9.95×10^{-4} m^2/s and 6.64 m^2/s, respectively. For case 1, the parameters are also the same except for the permeability of the hosting rock, which is 23 mD, leading to a hydraulic diffusivity $D_h = 0.03$ m^2/s. The rationale behind the choice of this value is explained in section 4.2. For all cases, a plane strain assumption is made.

3.2 Step 2 for Seismological Modeling

The next step is to set up the *DF* for the seismological modeling, see figure 3, and this involves two sub-steps, see equation (42). Take cases 2 and 3 for example, the first sub-step is to approximate the *LSDF* shown in figure 2a with a $\widehat{LSDF}$ as the subset A, see figure 3a, by honoring the original locations and orientations. The second sub-step is to construct a *SSSF* in the hosting rock as the subset B, see figure 3b; in principle, this can be derived from a statistical model if data is available (Jin & Zoback, 2015b). In this example, for simplicity and this does not change the generality of the method, I assign only one fracture to each element center shown in figure 2b as the modeling of fracture locations; for subset A, the orientations are the same as the associated deterministic fracture; for subset B, the orientations are randomly generated following a uniform distribution on [0, 360°]. Subsets A and B constitute the complete *DF* for the seismological modeling, see figure 3c. In this process, the fracture length is generated following a well-established scaling relation, which states that the number of fractures within a

natural fracture system scales with the fracture length according to a power law (e.g., Watanabe & Takahashi, 1995; Bonnet et al., 2001; Johri & Zoback, 2014):

$$N = CL^{-D} \tag{50}$$

where N is the number of fractures of length L, C is a site-specific constant and D is the so-called *fractal dimension* and a typical value is between 1 and 2. In this study, C=1.6861 and D=1.0015 (further details in section 4.4.2). The generated L is randomly distributed to all fractures shown in figure 3c.

On the other hand, the base scenario case 1 is designed not to include any fractures. Instead, the concept of random critical pore pressure (Shapiro et al., 2005) pre-allocated at seismicity seeds is adopted here. Nevertheless, such seeds can be explicitly visualized as equivalent fractures. The magnitude of the critical pore pressure translates to the fracture orientation with respect to the initial stress state. For calculating source parameters, fracture length is also randomly assigned. Therefore, the above two sub-steps are repeated for case 1. For meaningful comparisons, the locations of the seeds are identical to those in cases 2 and 3. In the first sub-step, however, equivalent fracture orientations are random and generated following a uniform distribution. The resulting two subsets of fractures are shown in figures 3d and 3e and the complete *DF* is shown in figures 3f.

In all cases, μ_s=0.6, μ_d=0.4 and a homogenous initial stress tensor $\boldsymbol{\sigma}'_0 = \boldsymbol{\sigma}'_{f0}$ = [15 0; 0 5.05] MPa is used. The initial effective normal stress and shear stress on all fractures are then calculated, forming a Mohr circle, see figure 4a, where the color indicates the associated initial Coulomb stress CFF_0. The same color scale is used in figure 3 to show the susceptibility of a fracture to slip with respect to $\boldsymbol{\sigma}'_{f0}$. The peak and residual frictional strengths, calculated from μ_s and μ_d, respectively, are also shown in figure 4a. Figure 4a also indicates that the domain is nearly critically stressed. Figures 4b and 4c show the distribution of CFF_0, which is no longer uniform, despite a uniform distribution of the fracture orientation.

4. Results

4.1 Fluid Pressure, Poroelastic Stress and Seismicity

Figures 5 shows four snapshots of the distribution of δp_p (figures 5a-5d) and the associated seismicity (figures 5e-5h) for case 1. The radial outward diffusion of δp_p with a smooth *overpressure front* (Shapiro et al., 1997) activates a subset of the pre-seeded seismicity sources where the equivalent critical pore pressure, $\mu_s \times CFF_0$, is breached by δp_p, leading to a similar radially progressive distribution in seismicity. Note here the "front" is a loose term and it refers to an isoline where changes in a quantity become visible. It is important to recognize that this case has one critical difference from the Shapiro et al. (2005) diffusion-only statistical model, that is, instead of using a pre-defined critical pore pressure value following a uniform distribution, it is the pre-defined fractures with uniformly distributed orientations that

are used. Because the orientation needs to be transformed through equation (1), the resulting CFF_0 and the equivalent critical pore pressure, $\mu_s \times CFF_0$, follow instead an exponential distribution, see figure 4b. Therefore, the modeled seismicity distribution here is indeed different. Also, the addition of the proposed seismological modeling framework further allows for the calculation of seismic source parameters, including M_w and $\Delta\tau$ as are shown in figures 5e-5h. Notice, however, that the modeled seismicity distribution fails to retain the evident linear feature of the pre-allocated source locations (figure 3f), illustrating a fundamental drawback of this approach.

Figure 6 shows the same snapshots of the same two quantities for case 2. Here, the effect of the *LSDF* (figure 2a) becomes evident. First, δp_p increases primarily along those fractures and secondarily within the hosting rock, leading to a highly non-smooth overpressure front (figures 6a-6d). Compared to case 1, δp_p here is of lower magnitude due to the *LSDF* diverting the fluid from the injector. Such a distribution leads to clear linear clustering of seismicity (figures 6e-6h), a phenomenon frequently observed in the field (e.g., Baisch & Harjes, 2003; Stabile et al., 2014; Deichmann et al., 2014; Block et al., 2015; Chen et al., 2018; Currie et al., 2018). Second, the distribution of seismicity is not coincident with that of δp_p, instead, the clustering occurs only along certain fractures. By further examining the fracture orientation (figure 3a), it can be seen that the seismicity is clustered near those that are well-oriented or sub-well-oriented with respect to $\boldsymbol{\sigma}'_0$ (or $\boldsymbol{\sigma}'_{f0}$) and meanwhile subjected to sufficient δp_p.

Figure 7 shows the results for case 3. The distribution of δp_p (figures 7a-7d) and the seismicity (figures 7q-7t) are shown together with three poroelastic stress invariants $I_1'/3$ (figures 7e-7h), $\sqrt{J_2'}$ (figures 7i-7l) and *MC* (figures 7m-7p). Recall all three quantities are calculated from $\delta\boldsymbol{\sigma}'_p$ under plane strain as discussed in section 2.3.3. Here, compared to case 2, complex effects of poroelastic coupling are elucidated. First, the distribution of δp_p is visibly different; the front of δp_p is suppressed and the magnitude is noticeably lower. Second, the poroelastic normal stress $I_1'/3$ develops, dominantly being extensional near the fluid-penetrated fractures; however, the magnitude of $I_1'/3$ is lower than that of its counterpart from the decoupled approach which predicts $I_1'/3 \approx -0.67\delta p_p$ (appendix A.1) using δp_p from case 2. Third, a pronounced shear stress field $\sqrt{J_2'}$ also develops and influences an even larger portion of the domain beyond the region subjected to $I_1'/3$ and δp_p, whereas its counterpart in case 2 is 0. Fourth, as a result, the distribution of *MC* is different than its counterpart in case 2, which is 0.34 δp_p (appendix A.1). Specifically, within the δp_p front (delineated in case 2, not case 3), the magnitude is lower; outside the δp_p front, it still prevails. This observation has important implications: within the fluid-pressurized region (i.e., in the near field), poroelastic coupling tends to inhibit seismicity; outside this region (i.e., in the far field), it can either remotely promote or inhibit seismicity depending on the fracture orientation. The reason behind the former is that a fracture within the fluid-pressurized region acts as preferred flow channel, leading to a discontinuous equivalent body force ($-\alpha\nabla\delta p_p$) acting away from it on the two sides, and therefore, inhibiting shear mode failure by unclamping it (Chang & Segall, 2016a; Jin & Zoback,

2016b; Jin & Zoback, 2017). This is reflected by the modeled seismicity. Like in case 2, here the seismicity is clustered near fractures favorably oriented with respect to $\boldsymbol{\sigma}'_0$ (or $\boldsymbol{\sigma}'_{f0}$) and meanwhile subjected to sufficient excess shear stress. Notice the linear clustering is further enhanced by poroelastic coupling. More importantly, the number of events in the near field is substantially reduced. Overall, the event population is reduced to only around a third of that in case 2. These observations are further elaborated in sections 4.2 and 4.3.1.

4.2 Spatial-Temporal Characteristics in the *R*-*T* Space

4.2.1 Fluid Pressure and Poroelastic Stress

The spatial-temporal characteristics of the modeled quantities are further illustrated using the so-called *R*-*T* plot, where *R* is the distance from the origin and *T* is the time since the beginning of the injection. The *R*-*T* plots of δp_p for cases 1-3 are given by figure 8. Overlaying are several iso-diffusivity profiles (gray dashed lines) calculated as $R=\sqrt{4\pi D_h T}$ +5m where D_h is the hydraulic diffusivity; $\sqrt{4\pi D_h T}$ is a characteristic profile derived from linear diffusion from a Heaviside point source injection in an isotropic, homogeneous and porous-only medium, and it is referred to as the *seismicity triggering front* (Shapiro et al., 1997; Shapiro et al., 2002). Notice the use of such profiles should apply only to case 1 (figure 8a). Nonetheless, for reference, they are also plotted for cases 2 and 3 (figures 8b, 8c), where additionally, the green and magenta lines corresponding to D_h of the hosting rock and the *LSDF*, respectively, are also plotted. It is mentioned in section 3.1 that in case 1, D_h = 0.03 m^2/s. This value is chosen such that the modeled δp_p front in the *R*-*T* space is approximately the same as that in case 2. In a sense, this value reflects the overall *effective* D_h of the fractured porous media in case 2. Case 1 shows a smooth variation of δp_p in the *R*-*T* space. In case 2, however, due to effect of fractures, the variations become non-smooth, in addition to an overall reduction in the magnitude of δp_p. The effect of poroelastic coupling is reflected by comparing case 2 and 3. The δp_p front is slightly suppressed and the magnitude of δp_p is further reduced.

To further illustrate the effect of poroelasic coupling in case 3, here I investigate the *R*-*T* characteristics of the poroelastic stress invariants, see figure 9. Although the spatial distributions of $I_1'/3$ and δp_p differ (figures 7a-7h), the delineated fronts of $I_1'/3$ (figure 9a) and δp_p (figure 8c) coincide in the *R*-*T* space. This is explained by equation (27), which states that $I_1'/3$, which scales linearly with the volumetric strain $\nabla\cdot\underline{u}_p$, diffuses together with δp_p. Poroelastic coupling does, however, reduce the magnitude of $I_1'/3$ compared to its counterpart $-0.67p$ (appendix A.1) where δp_p is given by figure 8b. The effect of poroelastic coupling further manifests itself in figure 9b, which shows the development of $\sqrt{J_2'}$ one-order of magnitude below *p*. This cannot be predicted by case 2. Also, it is evidently shown that the delineated front of $\sqrt{J_2'}$ well exceeds those of *p* and $I_1'/3$ (figures 8c and 9a). Figure 9c results from the combination

of figures 9a and 9b. The effect of poroelastic coupling is reflected by its difference in magnitude from its counterpart 0.34p (appendix A.1) where δp_p again is given by figure 8b.

4.2.2 Seismicity

Figures 10 shows the R-T distribution of the seismicity for cases 1-3 and the color indicates CFF_0. In figure 10a, a parabolic seismicity front is clearly delineated for case 1, showing also an evident "lag" behind the δp_p front (figure 8a). This lag reflects the effect of the initials stress with respect to the static shear failure line (i.e., the peak strength, see figure 4). Here D_h corresponding to the δp_p front and the seismicity front are 0.03 m^2/s and 0.015 m^2/s, respectively. In this case, if the seismicity front was to be used to back calculate D_h (e.g., Shapiro et al., 2002), D_h would be over-estimated by 100%. This motivates some nonlinear diffusion-based interpretations which incorporate pressure-dependent D_h (e.g., Hummel & Shapiro, 2012; Hummel & Shapiro, 2013). Here, my model is mechanics-based and it does not require the somewhat equivocal definition of "relatively large" pressure which underlines the diffusion-only statistical models (Shapiro et al., 1997). The effect of the *LSDF* can be seen in figure 10b. Notice the increased curvature of the parabolic seismicity front, which is above the predicted characteristic profile (second grey dashed line from the top) earlier and near the injector but below this profile later and away from the injector. Hummel & Shapiro (2013) used a power-law type of pressure-dependent D_h to correct for this change. However, my model not only produces this change but also introduces additional heterogeneity. Figure 10c shows further variations by accounting for poroelastic coupling. Compared to figure 10b, here the number of events is greatly reduced, the heterogeneity becomes much more pronounced, and some "outliers" are present. These are remotely triggered events to be elaborated in section 4.3.1. Additionally, nearly all events are sourced from favorably oriented fractures. The result of case 3 also shows qualitative agreement with a dataset provided in Hummel & Shapiro (2013).

4.3 Event Analysis

4.3.1 Near-Field and Remote Events (Coupled Case 3)

As has been discussed in section 4.2, poroelstic coupling tends to inhibit seismicity in the fluid-pressurized area but is also capable of triggering events remotely. Such effects are further illustrated here. To this end, the pressure front used here is defined as an iso-line on which δp_p is 1% of the maximum pressure, which is the prescribed constant injection pressure p_g in this study. The pressure front demarcates the near field and the far field, the latter assumed devoid of any pressure influence. Seismicity outside the pressure front is considered remotely triggered by only the remote poroelastic stress that is simply defined as the excess poroelastic shear stress outside the pressure front,

$$RS := H\left(0.01p_g - \delta p_p\right)MC \tag{51}$$

where H is the Heaviside function, MC is given by equation (37), and p_g is the fluid Dirichlet boundary condition (i.e., injection pressure in this study).

Figures 11a – 11h are eight time slices illustrating the evolution of remote events (blue) occurring in the far field (area colored by remote stress) in relation to the remaining events (magenta) located within the near field (non-colored area). In each time slice, only events occurred at that time are shown. Over time, poroelastic coupling inhibits near-field events and reduces their population while increasingly triggering more events remotely. This transition of triggering style is further shown by figure 11i where the relative sizes of the remote and near-field event populations are compared. Finally, figure 11j is the corresponding *R-T* plot of the remote poroelastic stress superposed with near-field and remote seismicity. The space-time is partitioned into two regimes, one dominated by remote triggering and the other, near-field triggering. The transition, however, is non-smooth due to the presence of the *LSDF*.

4.3.2 Repeating Events

The detection of repeating events in induced seismicity catalogs have been documented by many studies across scales (e.g., Baisch & Harjes, 2003; Moriya et al., 2003; Deichmann et al., 2014; Lengliné et al., 2014; Duverger et al, 2015; Zaliapin & Ben-Zion, 2016; Hakso & Zoback, 2017; Cochran et al., 2018). Identification of repeaters requires using cross correlation measurements to locate hypocenters as well as robustly constraining rupture dimensions (e.g., Ellsworth & Bulut, 2018). Admittedly, true repeaters with centroid separations less than rupture dimensions are difficult to search for, especially in small-magnitude event catalogs. Nevertheless, they can be theoretically predicted. Indeed, the proposed modeling framework here offers a natural way to modeling repeaters - shear stress loss on and around a source fault can be compensated by poroelastic stress, provided with right combinations of fault orientations and porolastic stressing history, and this process can be driven through multiple seismic cycles. This theory is especially suited for induced seismicity where fluid clearly plays a role. Here, the modeled repeater groups are shown figure 12. Each location indicates a doublet pair or a multiplet group (e.g., Poupinet et al., 1984; Waldhauser & Ellsworth, 2002) which contains two or more events that occur on the same source location but at different time; for visibility, a small-magnitude event is always plotted within a big-magnitude one (see the concentric circles). The repeating events exhibit some characteristics in space similar as those discussed in section 4.1. For example, the overall distribution is radial in case 1 but are clustered near favorably oriented fractures subjected to sufficient δp_p in case 2 and MC in case 3. Despite the difference in the spatial pattern, the number of repeater groups and the total number of events are similar between cases 1 and 2. In case 3, however, both drop significantly, suggesting poroelastic coupling inhibits the occurrence of repeating events as it does to the overall seismicity. Finally, within each group, an earlier event does not necessarily have a larger magnitude; the contrary is not uncommon. This is due to the complex stress path and the non-full degree of stress drop as is reflected by the r in equation (46). To see this, for each case, I chose one representative fracture that has generated the most

repeating events and plot the associated complete stress path colored with time, see figure 13. In each case, δp_p or *MC* suffice to drive a fracture through multiple seismic cycles within 90 minutes. However, the decoupled approach tends to over-predict both the number of seismic cycles and the number of repeater groups. Notice the increasingly unfavorable orientation of the fracture from cases 3 to 1. Additionally, within each seismic cycle, poroelastic coupling leads to a nonlinear stress path in case 3 as opposed to a linear leftward one in case 1 or 2.

Additionally, I analyze the number of events within each group and the associated inter-event time (i.e., inter-seismic time), see figure 14. From figures 14a, 14c and 14e, one observes that in all cases, the repeating events are primarily doublet pairs; multiplet groups are present, and the number of events within these groups suggests that δp_p can drive a fracture through up to 8 seismic cycles within the simulated 90 minutes of injection; this number is reduced if poroelastic coupling is considered. For the entire catalog, the inter-event time between any two consecutive repeating events are compiled. The results are plotted in figures 14b, 14d and 14f and they all exhibit a Poisson distribution described by $Pr=e^{-\lambda}\lambda^t/(t!)$, where Pr is the probability density function, λ is the average number of repeating events per time interval and t is the time interval (here I acknowledge a slight violation in notation; λ also means the Lame's constant in equation (48)). Observations of such distributions have also been reported for real datasets (e.g., Langenbruch et al., 2011; Cochran et al., 2018). The best-fitting λ with a 95% confidence and the associated probability density function are shown in figure 15. Overall, variations appear small among the cases, suggesting insignificant impact of fractures and poroelastic coupling on the inter-event time.

4.3.3 Triggered and Induced Events

In figure 1, the distinction between triggered and induced events is made based on the initial stress on a fracture in relation to its peak and residual frictional strengths. This is a quantitative definition and it reads

$$\begin{aligned} \sqrt{\left\|\boldsymbol{\sigma}'_{f0}\cdot\underline{n}_f\right\|^2-\left(\boldsymbol{\sigma}'_{f0}:\underline{n}_f\otimes\underline{n}_f\right)^2}&\le\mu_d\left(\boldsymbol{\sigma}'_{f0}:\underline{n}_f\otimes\underline{n}_f\right),\quad \textit{induced}\\ \mu_d\left(\boldsymbol{\sigma}'_{f0}:\underline{n}_f\otimes\underline{n}_f\right)<\sqrt{\left\|\boldsymbol{\sigma}'_{f0}\cdot\underline{n}_f\right\|^2-\left(\boldsymbol{\sigma}'_{f0}:\underline{n}_f\otimes\underline{n}_f\right)^2}&\le\mu_s\left(\boldsymbol{\sigma}'_{f0}:\underline{n}_f\otimes\underline{n}_f\right),\quad \textit{triggered} \end{aligned} \tag{52}$$

Equation (52) states that from a loading point of view, the key difference between the two lies in that an induced event represents shear failure on a fault that is otherwise tectonically inactive with respect to the background stress state, whereas a triggered event is indicative of a fault that is nevertheless expected to produce an earthquake given the background stress state but the process towards failure is favorably accelerated. This definition is consistent with the qualitative one provided by McGarr & Simpson (1997). As a result, upon seismicity, a triggered event releases a substantial amount of tectonic stress whereas an induced event releases mostly anthropogenic stress.

The triggered and induced events are distinguished from each other according to the above definition. The results are shown in figure 16. In cases 1-3, 93.3%, 92.8% and 98.5% of the events are triggered; the remaining small number of events are induced and are distributed in close proximity to the injector, as they occur on unfavorably-oriented fractures and require a significant amount of δp_p or *MC* to be activated. Again, for either type of event, accounting for the *LSDF* leads to the clustering and accounting for poroelastic coupling significantly reduces the number of events.

4.4 Source Parameters

4.4.1 Stress Drop, Fracture Length and Moment Magnitude

Figures 17a, 17c and 17e summarize the modeled seismic source characteristics in the parameter space for cases 1-3. For each event, M_w is plotted against the associated fracture length L and colored with $\Delta\tau$. The modeled events, with M_w between -3 and -1, occur on fractures of L ranging from 0.1m and 10m, and $\Delta\tau$ ranges from below 0.1 MPa to above 1 MPa, consistent with many real induced micro-earthquake datasets at a similar scale (e.g., Goertz-Allmann et al., 2011; Mukuhira, 2013). Such source characteristics overall seem not affected by the *LSDF* nor poroelastic coupling. For a realistic range of $\Delta\tau$, the parameter r in equation (46) turns out to be a key controlling factor and the sensitivity of model outcomes to r remains to be explored. I will leave this for future work. Figures 17b, 17d and 17f further show the overall similar distribution of $\Delta\tau$ for cases 1-3. In each case, [0.1, 1] MPa is the dominant range. Notice, however, that case 3 sees a bigger portion of events with higher $\Delta\tau$ (e.g., above 1 MPa). The reason underlies nonlinear poroelastic loading paths with upward components, which lead to larger $\Delta\tau_{max}$ (equation (47)) compared to decoupled cases, see also figures 1 and 13c.

4.4.2 Magnitude-Frequency Scaling

I have introduced a power law that describes the commonly observed scaling relation between the fracture length and the frequency (section 3.2). Meanwhile, earthquakes in nature are characterized with a universal statistical relation between the magnitude and the cumulative frequency, namely the Gutenberg-Richter law (Gutenberg, 1956), which reads:

$$\lg N(m > M_w) = a - bM_w \tag{53}$$

where $N(m>M_w)$ is the total number of events with a moment magnitude m above M_w, and a and b are constants.

In nature, the fractal dimension D shown in equation (50) is observed to be mostly between 1 and 2 (e.g., Okubo & Aki, 1987). The b-value fitted from natural earthquake catalogs is commonly around 1 (e.g., Shi & Bolt, 1982) albeit a wide possible range of variations from 0.3 to 2.5, see, e.g., El-Isa & Eaton (2014) for a comprehensive review. Studies suggest that D and b are inherently related. For example, Hirata (1989) suggests a well-recognized $D = 2b$ relation. A somewhat curious yet common observation is that

for induced seismicity, especially microseismicity as is modeled here, *b*-value is frequently elevated above 1 and even 2 (e.g., Vermylen & Zoback, 2011; Bachmann et al., 2011; Bachmann et al., 2012; Eaton et al., 2014; Tutuncu & Bui, 2015; Mousavi et al., 2017; Chen et al., 2018; Brudzinski & Kozłowska et al., 2019), although a uni-modal distribution around 1 (Schoenball et al., 2015; Goertz-Allmann, 2017) and a bi-modal distribution around both 1 and 2 (Igonin et al., 2018; Kettlety et al., 2019) have also been reported.

In figure 18, for each case, the distribution of lengths of all fractures (figures 3c, 3f) is plotted (green), together with the power law fitting line (magenta); the distribution of lengths of the activated subset of fractures is also plotted (red), which clearly no longer obeys the power law decay, owing to that only favorably oriented fractures are induced to slip. Nonetheless, the magnitude-frequency scaling relation still holds for the induced events, as is illustrated in figure 19. For each case, the distribution of M_w, which primarily varies between -3.5 and -1.0, is shown as the histogram (yellow green); the total number of events (i.e., cumulative frequency) is shown by the blue-green dots, which is then used to fit the Gutenburg-Richter law, yielding a *b*-value around 2. Notice the similarities among all three cases in both figures 18 and 19, suggesting that the *b*-value is likely to be independent from the *LSDF* and poroelastic coupling. The breaking-down in the power law distribution of the length of the activated subset of fractures might be responsible for the deviation in the *b*-value for induced seismicity. Similar mechanical origins of the *b*-value elevation for induced seismicity have been suggested by other studies (Tafti et al., 2013; Stormo et al., 2015). In the end, the specific *b*-value might be jointly determined by the fracture network itself (Eaton et al., 2014; Afshari Moein et al., 2018), the poroelastic properties (Wangen, 2019) and the stress state (Scholz. 2015).

5.Summary and Conclusions

I have developed a hydro-mechanical-seismological modeling framework for fluid perturbation-induced seismicity in a fluid-saturated and arbitrarily fractured nonlinear poroelastic medium. Following predefined distributions characteristic of a natural fracture system, a dual network of fractures is generated consisting large-scale deterministic fractures (*LSDF*) and small-scale stochastic fractures (*SSSF*) within the hosting rock. The modeling consists two steps, including first the quasi-static fracture-poro-mechanical modeling and second the seismological modeling. In the first step, only the *LSDF* is resolved, using a fluid-solid fully coupled nonlinear computational poromechanical model customized for arbitrarily fractured media. This provides a *LSDF*-controlled full poroelastic stress tensor as a pivotal input for the second step, in which the complete dual network of fractures is then considered. The seismicity-induced shear stress loss on a source fracture is stochastically generated as a static quantity without explicitly modeling the co-seismic dynamic rupture; it is dictated by the full poroelastic stressing history in conjunction with the initial stress state. A prediction-correction type of fracture stress updating

scheme is developed accordingly and advanced in time to produce seismicity catalogs. Three progressive cases were designed to systematically showcase model capabilities as well as effects of fractures and full poroelastic coupling on the resulting fluid overpressure, solid stress as well as seismicity and its source characteristics. Compared to the prevalent fracture-free, coupling-free and diffusion-only class of statistical models, my model produces induced seismicity with more realistic spatial-temporal and statistical characteristics frequently seen in real data. It also goes beyond the scope of most current models and provides a synthetic catalog of induced events, allowing for analyzing seismic source characteristics and establishing connections between observations and model physics.

Several key new findings from the numerical experiments are highlighted here.

(1) The spatial-temporal evolution of the pore fluid overpressure δp_p, the change in the solid effective stress tensor $\delta\boldsymbol{\sigma}'_p$, the associated stress invariants I_1' and $\sqrt{J_2'}$ and the excess shear stress invariant $MC=\sqrt{J_2'}-sin(\phi)I_1'/3$, all differ in a porous medium, a fractured porous medium and a fractured poroelastic medium. In space, the presence of the hydraulically conductive *LSDF* leads to marked localization of these quantities around it. Poroelastic coupling tends to reduce the magnitude of δp_p and I_1' near fluid-penetrated fractures but also predicts an otherwise non-existing $\sqrt{J_2'}$ within the entire domain. As a result of, *MC* is reduced in the near field but increased in the far field. In the *R*-*T* space, δp_p and I_1' share the same front which is below the front shared by $\sqrt{J_2'}$ and *MC*.

(2) In space, the *LSDF* leads to not only heterogeneity but also pronounced linear clustering in seismicity. The clustering occurs only near fractures favorably oriented with respect the initial stress and meanwhile subjected to sufficient excess shear stress. Poroelastic coupling further enhances the clustering; more importantly, because of the way it generates the excess shear stress, poroelastic coupling inhibits seismicity in the near field and promotes events remotely in the far field. The style of triggering is dominated by near-field triggering at an earlier time and transitions into remote triggering-dominated subsequently. Overall, poroelastic coupling significantly reduces the event population.

(3) External fluid perturbations and internal seismicity are the two sources driving stress changes, and together they can drive a source fracture through multiple seismic cycles on a time scale relevant to the problem. This provides a viable mechanism of fluid-induced repeating events with characteristic stepwise stress paths. Poroelastic coupling, however, tends to inhibit the occurrence of repeaters as it does to the overall seismicity, in addition to adding nonlinearity to the associated stress paths.

(4) Although collectively referred to as induced seismicity, the modeled events are indeed predominantly triggered events rather than induced events. Because the latter are sourced on unfavorably-oriented fractures that require significant excess shear stress, they concentrate near the source of fluid perturbations.

(5) Some statistical characteristics of induced seismicity appear to remain independent from the *LSDF* and poroelastic coupling. For the given set of parameters, the inter-event time between two consecutive repeater follows a Poisson's distribution, the stress drop $\Delta\tau$ predominantly falls in between 0.1 MPa and 1 MPa obeying overall similar distributions and the *b*-value in the magnitude-frequency scaling relation is consistently around 2, irrespective of the case. However, poroelastic coupling does favor higher $\Delta\tau$ due to its upward bending of the stress path, leading to some slight differences in the distributions of $\Delta\tau$ and M_w near the end of their distribution intervals.

(6) In the complete dual fracture system, the fracture length and the frequency obey a realistic power law scaling relation with a characteristic fractal dimension; however, this relation breaks down for the activated subset of fractures since only favorably-oriented fractures are induced to slip. This mechanical origin might explain the curious deviation of the *b*-value from 1 to above 2 as has been commonly seen in induced seismicity catalogs.

Acknowledgement

I thank Norm Sleep, William Ellsworth and Apostolos Sarlis for discussion. The work is partially funded by the Stanford Center for Induced and Triggered Seismicity. No data were used in producing this manuscript.

Appendix

A.1 Equivalent Poroelastic Stress Invariants for Cases 1 & 2

For case 3, equations (35) - (37) are used to calculate $I_1'/3$, $\sqrt{J_2'}$ and *MC* shown in figure 7. For cases 1 and 2 without the coupling effect, the pressure changes within the hosting from external fluid perturbations can be translated to an equivalent change in its effective normal stress change as $\alpha\delta p_p\mathbf{1}$. This is similar to equation (3) except for the use of Biot-Willis coefficient of the hosting rock. Substituting it into equations (35) and (36) yields the following equivalent poroelastic stress invariants,

$$\frac{1}{3}I_1' = -\frac{2}{3}(1+\nu)\alpha\delta p_p \tag{A1}$$

$$\sqrt{J_2'} = 0 \tag{A2}$$

Given the parameters used in this study, specifically, $\nu = 0.25$, $\alpha = 0.8$ and $\mu_s = 0.6$, equation (A1) predicts that $I_1'/3 \approx -0.67\delta p_p$ and $MC=\sqrt{J_2'}-sin(\phi)I_1'/3 \approx 0.34\delta p_p$ for cases 1 and 2.

Nomenclature

1. Domains	
Ω_f, Ω_m	fracture domain and hosting rock (matrix) domain
$\partial\Omega_f$	fracture domain boundary
∂f	fracture-hosting rock interface (also dimensionally reduced fracture domain)
Ω, $\overline{\Omega}$	bulk model domain and its mixed-dimensional representation
LSDF, $\widetilde{LSDF}$	a large-scale deterministic fracture network and its discrete approximation
SSSF	a small-scale stochastic fracture network
DF	a dual-scale fracture network
F_I, N	I^{th} large-scale deterministic fracture in *LSDF*, total population
f_a, n_a	a^{th} discrete fracture in $\widetilde{LSDF}$, total population
f_b, n_b	b^{th} discrete fracture in *SSSF*, total population
2. Fracture domain properties & variables	
CFF	Coulomb Failure Function (Coulomb stress), Pa
$\lvert\tau_f\rvert$, $\lvert\tau_{f0}\rvert$	current and initial maximum shear stress, Pa
$\lvert\tau_{f0}+\delta\tau_f\rvert$	current maximum shear stress showing decompositions, Pa
σ'_{nf}, σ'_{nf0}, $\delta\sigma'_{nf}$	current, initial and perturbing effective normal stress, Pa
$\underline{n_f}$	unit normal vector, [-]
μ_s, μ_d	static and dynamic frictional coefficients, [-]
$\boldsymbol{\sigma}_f$	current Cauchy total stress tensor, Pa
$\boldsymbol{\sigma}'_f$, $\boldsymbol{\sigma}'_{f0}$, $\delta\boldsymbol{\sigma}'_f$	current, initial and perturbing effective stress tensors, Pa
$\delta\boldsymbol{\sigma}'_{fp}$, $\delta\boldsymbol{\sigma}'_{fs}$	changes in the effective stress tensor due to external fluid perturbations and seismicity, Pa
$\delta\sigma'_{fxx}$, $\delta\sigma'_{fyy}$, $\delta\sigma'_{fzz}$	normal components of $\delta\boldsymbol{\sigma}'_f$, Pa
$\delta\sigma'_{fxy}$, $\delta\sigma'_{fxz}$, $\delta\sigma'_{fyz}$	shear components of $\delta\boldsymbol{\sigma}'_f$, Pa
p_f, p_{f0}, δp_f	current and initial fluid pressure and fluid overpressure, Pa
δp_{fp}, δp_{fs}	fluid overpressure due to external fluid perturbations and seismicity, Pa
b_0	initial hydraulic aperture, m
C_f	compressibility, Pa^{-1}
$\Delta\tau_j$, $\Delta\tau_{jmax}$	static shear stress drop from the j^{th} episode of slip and its maximum likely value, Pa
r	a random variable, [-]
L, W	length and width, m
D	fractal dimension, [-]
C	a site-specific parameter for characterizing fracture length distributions, [-]
3. Porous hosting rock (matrix) domain properties & variables	
K_m	bulk modulus of solid grains/skeleton, Pa
K_b	bulk modulus, Pa

α	Biot-Willis coefficient, [-]
ϕ_{m0}	initial porosity, [-]
C_m	compressibility, Pa^{-1}
λ, μ	Lame's constant and shear modulus, Pa
ϕ	frictional angle, °
$\mathbf{k}_m$	permeability tensor, m^2
$\boldsymbol{\sigma}$, $\boldsymbol{\sigma}_0$, $\delta\boldsymbol{\sigma}$	current, initial and perturbing Cauchy total stress tensors, Pa
$\delta\boldsymbol{\sigma}_p$, $\delta\boldsymbol{\sigma}_s$	changes in the Cauchy total stress tensor due to external fluid perturbations and seismicity, Pa
$\delta\boldsymbol{\sigma}'_p$, δp_p	changes in the effective stress tensor and fluid overpressure due to external fluid perturbations, Pa
I_1', $\sqrt{J_2'}$	first and second poroelastic stress invariants, Pa
MC	excess poroelastic shear stress, Pa
RS	remote poroelastic stress, Pa
$\delta\underline{u}_p$	change in the displacement vector due to external fluid perturbations, m
$\mathbf{D}$	elastic stiffness tensor, Pa

4. Other properties and variables

$\underline{v}$	fluid velocity vector, m/s
η	fluid viscosity, Pa·s
s	external fluid source/sink term divided by the initial fluid density, s^{-1}
Λ_0	geometric factor reflecting effects of fractures on medium fluid storage capacity, [-]
p_g	fluid Dirichlet boundary value (injection pressure), Pa
M_0	seismic moment, N·m
M_w	moment magnitude, [-]
a, b	Gutenberg-Richter constants, [-]

5. Numerical discretization (fractures)

$\mathbf{M}_{F_I}$	fluid storage capacity matrix of the I^{th} large-scale deterministic fracture
$\mathbf{K}_{F_I}$	hydraulic conductivity matrix of the I^{th} large-scale deterministic fracture

6. Numerical discretization (hosting rock/matrix)

$\tilde{\mathbf{M}}$, $\mathbf{M}$	fluid storage capacity matrix in the absence and presence of fractures
$\mathbf{K}$	hydraulic conductivity matrix
$\mathbf{C}$	coupling matrix
$\mathbf{G}$	elastic stiffness matrix
$\mathbf{Q}$	a matrix for extracting fracture nodal pressure from matrix nodal pressure in a hybrid-dimensional approach
$\mathbf{B}$	standard finite element displacement-strain transformation matrix

$\hat{\zeta}_p$, $\underline{d}_p$	nodal values of δp_p and $\delta \underline{u}_p$
$\underline{F}_1$, $\underline{F}_2$, $\underline{F}_3$	external nodal mass vectors
$\underline{Y}$	external nodal force vector
$\underline{R}_2$, $\underline{R}_3$	residual vectors
7. Math operators & identities	
$tr(\cdot)$	trace (diagonal sum)
$H(\cdot)$	Heaviside function
∇, $\nabla^{(s)}$, ∇_τ	gradient, symmetric gradient and tangential gradient operators
$\nabla\cdot$	divergence operator
$\cdot$	dot product
:	double tensor contraction
$\otimes$	Dyadic product
1	unit identity (Kronecker delta)

Reference

Afshari Moein, M. J., Tormann, T., Valley, B., & Wiemer, S. (2018). Maximum magnitude forecast in hydraulic stimulation based on clustering and size distribution of early microseismicity. *Geophysical Research Letters*, *45*(14), 6907-6917.

Gómez Alba, S., Vargas, C. A., & Zang, A. (2020). Evidencing the relationship between injected volume of water and maximum expected magnitude during the Puerto Gaitán (Colombia) earthquake sequence from 2013 to 2015. *Geophysical Journal International*, *220*(1), 335-344.

Almakari, M., Dublanchet, P., Chauris, H., & Pellet, F. (2019). Effect of the Injection Scenario on the Rate and Magnitude Content of Injection‐Induced Seismicity: Case of a Heterogeneous Fault. *Journal of Geophysical Research: Solid Earth*, *124*(8), 8426-8448.

Altmann, J. B., Müller, B. I. R., Müller, T. M., Heidbach, O., Tingay, M. R. P., & Weißhardt, A. (2014). Pore pressure stress coupling in 3D and consequences for reservoir stress states and fracture reactivation. *Geothermics*, 52, 195-205.

Andrews, D. J. (1976). Rupture velocity of plane strain shear cracks. *Journal of Geophysical Research*, *81*(32), 5679-5687.

Angus, D. A., Kendall, J. M., Fisher, Q. J., Segura, J. M., Skachkov, S., Crook, A. J. L., & Dutko, M. (2010). Modelling microseismicity of a producing reservoir from coupled fluid-flow and geomechanical simulation. *Geophysical Prospecting*, 58(5), 901-914.

Bachmann, C. E., Wiemer, S., Goertz‐Allmann, B. P., & Woessner, J. (2012). Influence of pore‐pressure on the event‐size distribution of induced earthquakes. *Geophysical Research Letters*, *39*(9).

Bachmann, C. E., Wiemer, S., Woessner, J., & Hainzl, S. (2011). Statistical analysis of the induced Basel 2006 earthquake sequence: introducing a probability-based monitoring approach for Enhanced Geothermal Systems. *Geophysical Journal International*, *186*(2), 793-807.

Baisch, S., & Harjes, H. P. (2003). A model for fluid-injection-induced seismicity at the KTB, Germany. *Geophysical Journal International*, *152*(1), 160-170.

Baisch, S., Vörös, R., Rothert, E., Stang, H., Jung, R., & Schellschmidt, R. (2010). A numerical model for fluid injection induced seismicity at Soultz-sous-Forêts. *International Journal of Rock Mechanics and Mining Sciences*, 47(3), 405-413.

Barbour, A. J., Norbeck, J. H., & Rubinstein, J. L. (2017). The effects of varying injection rates in Osage County, Oklahoma, on the 2016 M w 5.8 Pawnee earthquake. *Seismological Research Letters*, *88*(4), 1040-1053.

Berkowitz, B. (2002). Characterizing flow and transport in fractured geological media: A review. *Advances in Water Resources*, 25(8), 861-884.

Biot, M. A. (1941). General theory of three‐dimensional consolidation. *Journal of applied physics*, *12*(2), 155-164.

Block, L. V., Wood, C. K., Yeck, W. L., & King, V. M. (2015). Induced seismicity constraints on subsurface geological structure, Paradox Valley, Colorado. *Geophysical Journal International*, *200*(2), 1172-1195.

Bonnet, E., Bour, O., Odling, N. E., Davy, P., Main, I., Cowie, P., & Berkowitz, B. (2001). Scaling of fracture systems in geological media. *Reviews of Geophysics*, *39*(3), 347-383.

Booker, J. R., & Carter, J. P. (1986). Analysis of a point sink embedded in a porous elastic half space. *International Journal for Numerical and Analytical Methods in Geomechanics*, *10*(2), 137-150.

Borja, R. I. (2006). On the mechanical energy and effective stress in saturated and unsaturated porous continua. *International Journal of Solids and Structures*, *43*(6), 1764-1786.

Borja, R. I. (2013). *Plasticity: modeling & computation*. Berlin: Springer.

Brudzinski, M. R., & Kozłowska, M. (2019). Seismicity induced by hydraulic fracturing and wastewater disposal in the Appalachian Basin, USA: a review. *Acta Geophysica*, *67*(1), 351-364.

Byerlee, J. (1978). Friction of rocks. In *Rock friction and earthquake prediction* (pp. 615-626). Basel: Birkhäuser.

Carcione, J. M., Currenti, G., Johann, L., & Shapiro, S. (2018). Modeling fluid injection induced microseismicity in shales. *Journal of Geophysics and Engineering*, *15*(1), 234.

Carcione, J. M., Da Col, F., Currenti, G., & Cantucci, B. (2015). Modeling techniques to study CO2-injection induced micro-seismicity. *International Journal of Greenhouse Gas Control*, *42*, 246-257.

Chang, K. W., & Segall, P. (2016a). Injection‐induced seismicity on basement fractures including poroelastic stressing. *Journal of Geophysical Research: Solid Earth*, 121(4), 2708-2726.

Chang, K. W., & Segall, P. (2016b). Seismicity on basement fractures induced by simultaneous fluid injection–extraction. *Pure and Applied Geophysics*, 173(8), 2621-2636.

Chang, K. W., & Segall, P. (2017). Reduction of Injection-Induced Pore-Pressure and Stress in Basement Rocks Due to Basal Sealing Layers. *Pure and Applied Geophysics*, 174(7), 2649-2661.

Chang, K. W., & Yoon, H. (2018). 3‐D Modeling of Induced Seismicity Along Multiple Faults: Magnitude, Rate, and Location in a Poroelasticity System. *Journal of Geophysical Research: Solid Earth*, *123*(11), 9866-9883.

Chen, H., Meng, X., Niu, F., Tang, Y., Yin, C., & Wu, F. (2018). Microseismic monitoring of stimulating shale gas reservoir in SW China: 2. Spatial clustering controlled by the preexisting faults and fractures. *Journal of Geophysical Research: Solid Earth*, *123*(2), 1659-1672.

Cleary, M. P. (1977). Fundamental solutions for a fluid-saturated porous solid. *International Journal of Solids and Structures*, *13*(9), 785-806.

Cochran, E. S., Ross, Z. E., Harrington, R. M., Dougherty, S. L., & Rubinstein, J. L. (2018). Induced earthquake families reveal distinctive evolutionary patterns near disposal wells. *Journal of Geophysical Research: Solid Earth*, *123*(9), 8045-8055.

Cryer, C. W. A. (1963). A comparison of the three-dimensional consolidation theories of Biot and Terzaghi. *The Quarterly Journal of Mechanics and Applied Mathematics*, *16*(4), 401-412.

Currie, B. S., Free, J. C., Brudzinski, M. R., Leveridge, M., & Skoumal, R. J. (2018). Seismicity induced by wastewater injection in Washington County, Ohio: influence of preexisting structure, regional stress regime, and well operations. *Journal of Geophysical Research: Solid Earth*, *123*(5), 4123-4140.

Deichmann, N., Kraft, T., & Evans, K. F. (2014). Identification of fractures activated during the stimulation of the Basel geothermal project from cluster analysis and focal mechanisms of the larger magnitude events. *Geothermics*, *52*, 84-97.

Deichmann, N., Kraft, T., & Evans, K. F. (2014). Identification of faults activated during the stimulation of the Basel geothermal project from cluster analysis and focal mechanisms of the larger magnitude events. *Geothermics*, *52*, 84-97.

Dempsey, D., & Suckale, J. (2017). Physics ‐ based forecasting of induced seismicity at Groningen gas field, the Netherlands. *Geophysical Research Letters*, *44*(15), 7773-7782.

Deng, K., Liu, Y., & Harrington, R. M. (2016). Poroelastic stress triggering of the December 2013 Crooked Lake, Alberta, induced seismicity sequence. *Geophysical Research Letters*, 43(16), 8482-8491.

Dieterich, J. (1994). A constitutive law for rate of earthquake production and its application to earthquake clustering. *Journal of Geophysical Research: Solid Earth*, *99*(B2), 2601-2618.

Dieterich, J. H., Richards ‐ Dinger, K. B., & Kroll, K. A. (2015). Modeling injection ‐ induced seismicity with the physics ‐ based earthquake simulator RSQSim. *Seismological Research Letters*, *86*(4), 1102-1109.

Dunham, E. M., & Rice, J. R. (2008). Earthquake slip between dissimilar poroelastic materials. *Journal of Geophysical Research: Solid Earth*, *113*(B9).

Duverger, C., Godano, M., Bernard, P., Lyon ‐ Caen, H., & Lambotte, S. (2015). The 2003 – 2004 seismic swarm in the western Corinth rift: Evidence for a multiscale pore pressure diffusion process along a permeable fracture system. *Geophysical Research Letters*, 42(18), 7374-7382.

Eaton, D. W., Davidsen, J., Pedersen, P. K., & Boroumand, N. (2014). Breakdown of the Gutenberg ‐ Richter relation for microearthquakes induced by hydraulic fracturing: influence of stratabound fractures. *Geophysical Prospecting*, *62*(Vertical Seismic Profiling and Microseismicity Frontiers), 806-818.

El-Isa, Z. H., & Eaton, D. W. (2014). Spatiotemporal variations in the b-value of earthquake magnitude–frequency distributions: Classification and causes. *Tectonophysics*, *615*, 1-11.

Ellsworth, W. L., & Bulut, F. (2018). Nucleation of the 1999 Izmit earthquake by a triggered cascade of foreshocks. *Nature Geoscience*, *11*(7), 531-535.

Fan, Z., Eichhubl, P., & Gale, J. F. (2016). Geomechanical analysis of fluid injection and seismic fault slip for the Mw4. 8 Timpson, Texas, earthquake sequence. *Journal of Geophysical Research: Solid Earth*, *121*(4), 2798-2812.

Goebel, T. H. W., Weingarten, M., Chen, X., Haffener, J., & Brodsky, E. E. (2017). The 2016 Mw5. 1 Fairview, Oklahoma earthquakes: Evidence for long-range poroelastic triggering at> 40 km from fluid disposal wells. *Earth and Planetary Science Letters*, *472*, 50-61.

Goertz-Allmann, B. P., & Wiemer, S. (2012). Geomechanical modeling of induced seismicity source parameters and implications for seismic hazard assessment. *Geophysics*, *78*(1), KS25-KS39.

Goertz ‐ Allmann, B. P., Gibbons, S. J., Oye, V., Bauer, R., & Will, R. (2017). Characterization of induced seismicity patterns derived from internal structure in event clusters. *Journal of Geophysical Research: Solid Earth*, *122*(5), 3875-3894.

Goertz ‐ Allmann, B. P., Goertz, A., & Wiemer, S. (2011). Stress drop variations of induced earthquakes at the Basel geothermal site. *Geophysical Research Letters*, *38*(9).

Gutenberg, B. (1956). The energy of earthquakes. *Quarterly Journal of the Geological Society*, *112*(1-4), 1-14.

Hakso, A., & Zoback, M. (2017). Utilizing multiplets as an independent assessment of relative microseismic location uncertainty. *The Leading Edge*, *36*(10), 829-836.

Hanks, T. C., & Boore, D. M. (1984). Moment‐magnitude relations in theory and practice. *Journal of Geophysical Research: Solid Earth*, *89*(B7), 6229-6235.

Hardebol, N. J., Maier, C., Nick, H., Geiger, S., Bertotti, G., & Boro, H. (2015). Multiscale fracture network characterization and impact on flow: A case study on the Latemar carbonate platform. *Journal of Geophysical Research: Solid Earth*, 120(12), 8197-8222.

He, J., Rui, Z., & Ling, K. (2016). A new method to determine Biot's coefficients of Bakken samples. *Journal of Natural Gas Science and Engineering*, *35*, 259-264.

Hirata, T. (1989). A correlation between the b value and the fractal dimension of earthquakes. *Journal of Geophysical Research: Solid Earth*, *94*(B6), 7507-7514.

Hirthe, E. M., & Graf, T. (2015). Fracture network optimization for simulating 2D variable-density flow and transport. *Advances in Water Resources*, 83, 364-375.

Hopp, C., Sewell, S., Mroczek, S., Savage, M., & Townend, J. (2020). Seismic response to evolving injection at the Rotokawa geothermal field, New Zealand. *Geothermics*, *85*, 101750.

Hornby, B.E., The elastic properties of shales, Ph.D. dissertation, University of Cambridge, Cambridge, England, 1995.

Hughes, T. J. (2012). *The finite element method: linear static and dynamic finite element analysis*. Courier Corporation.

Hummel, N., & Shapiro, S. A. (2012). Microseismic estimates of hydraulic diffusivity in case of non-linear fluid-rock interaction. *Geophysical Journal International*, *188*(3), 1441-1453.

Hummel, N., & Shapiro, S. A. (2013). Nonlinear diffusion-based interpretation of induced microseismicity: A Barnett Shale hydraulic fracturing case study. *Geophysics*, *78*(5), B211-B226.

Igonin, N., Zecevic, M., & Eaton, D. W. (2018). Bilinear Magnitude‐Frequency Distributions and Characteristic Earthquakes During Hydraulic Fracturing. *Geophysical Research Letters*, *45*(23), 12-866.

Izadi, G., & Elsworth, D. (2014). Reservoir stimulation and induced seismicity: Roles of fluid pressure and thermal transients on reactivated fractured networks. *Geothermics*, *51*, 368-379.

Jin, L., & Zoback, M. D. (2015a). An Analytical Solution for Depletion-induced Principal Stress Rotations In 3D and its Implications for Fracture Stability. In *AGU Fall Meeting Abstracts*.

Jin, L., & Zoback, M. D. (2015b). Identification of fracture-controlled damage zones in microseismic data–an example from the Haynesville shale. *SEG Technical Program Expanded Abstracts 2015*, 726-730.

Jin, L., & Zoback, M. D. (2016a). Including a stochastic discrete fracture network into one-way coupled poromechanical modeling of injection-induced shear re-activation. In *50th US Rock Mechanics/Geomechanics Symposium*. American Rock Mechanics Association.

Jin, L., & Zoback, M. D. (2016b). Impact of Poro-Elastic Coupling and Stress Shadowing on Injection-Induced Microseismicity in Reservoirs Embedded With Discrete Fracture Networks. In *AAPG Annual Convention and Exhibition*.

Jin, L., & Zoback, M. D. (2017). Fully Coupled Nonlinear Fluid Flow and Poroelasticity in Arbitrarily Fractured Porous Media: A Hybrid‐Dimensional Computational Model. *Journal of Geophysical Research: Solid Earth*, *122*(10), 7626-7658.

Jin, L., & Zoback, M. D. (2018a). Modeling Induced Seismicity: Co-Seismic Fully Dynamic Spontaneous Rupture Considering Fault Poroelastic Stress. In *52nd US Rock Mechanics/Geomechanics Symposium*. American Rock Mechanics Association.

Jin, L., & Zoback, M. D. (2018b). Fully Dynamic Spontaneous Rupture Due to Quasi‐Static Pore Pressure and Poroelastic Effects: An Implicit Nonlinear Computational Model of Fluid‐Induced Seismic Events. *Journal of Geophysical Research: Solid Earth*, *123*(11), 9430-9468.

Jin, L., & Zoback, M. D. (2019). Depletion-Induced Poroelastic Stress Changes in Naturally Fractured Unconventional Reservoirs and Implications for Hydraulic Fracture Propagation. *In SPE Annual Technical Conference and Exhibition. Society of Petroleum Engineers.*

Johann, L., Dinske, C., & Shapiro, S. A. (2016). Scaling of seismicity induced by nonlinear fluid‐rock interaction after an injection stop. *Journal of Geophysical Research: Solid Earth*, *121*(11), 8154-8174.

Johri, M., Zoback, M. D., & Hennings, P. (2014). A scaling law to characterize fracture-damage zones at reservoir depthsFracture Damage Zones at Depth. *AAPG Bulletin*, *98*(10), 2057-2079.

Kanamori, H., & Anderson, D. L. (1975). Theoretical basis of some empirical relations in seismology. *Bulletin of the seismological society of America*, *65*(5), 1073-1095.

Keranen, K.M. & Weingarten, M. (2018). Induced Seismicity. *Annual Review of Earth and Planetary Sciences*. 46, 149-174.

Kettlety, T., Verdon, J. P., Werner, M. J., Kendall, J. M., & Budge, J. (2019). Investigating the role of elastostatic stress transfer during hydraulic fracturing-induced fault activation. *Geophysical Journal International*, *217*(2), 1200-1216.

Kroll, K. A., Richards‐Dinger, K. B., & Dieterich, J. H. (2017). Sensitivity of induced seismic sequences to rate‐and‐state frictional processes. *Journal of Geophysical Research: Solid Earth*, *122*(12), 10-207.

Langenbruch, C., & Zoback, M. D. (2016). How will induced seismicity in Oklahoma respond to decreased saltwater injection rates?. *Science advances*, *2*(11), e1601542.

Langenbruch, C., Dinske, C., & Shapiro, S. A. (2011). Inter event times of fluid induced earthquakes suggest their Poisson nature. *Geophysical Research Letters*, *38*(21).

Langenbruch, C., Weingarten, M., & Zoback, M. D. (2018). Physics-based forecasting of man-made earthquake hazards in Oklahoma and Kansas. *Nature communications*, *9*(1), 3946.

Lengliné, O., Lamourette, L., Vivin, L., Cuenot, N., & Schmittbuhl, J. (2014). Fluid‐induced earthquakes with variable stress drop. *Journal of Geophysical Research: Solid Earth*, *119*(12), 8900-8913.

Ma, X., & Zoback, M. D. (2017). Laboratory experiments simulating poroelastic stress changes associated with depletion and injection in low‐porosity sedimentary rocks. *Journal of Geophysical Research: Solid Earth*, *122*(4), 2478-2503.

Maillot, B., Nielsen, S., & Main, I. (1999). Numerical simulation of seismicity due to fluid injection in a brittle poroelastic medium. *Geophysical Journal International*, 139(2), 263-272.

Mandel, J. (1953). Consolidation des sols (étude mathématique). *Geotechnique*, *3*(7), 287-299.

McGarr, Arthur F. and Simpson, David (1997). A broad look at induced and triggered seismicity. *In: Rockbrust and seismicity in mines* (pp. 385-396). Rotterdam: Balkema.

Megies, T., & Wassermann, J. (2014). Microseismicity observed at a non-pressure-stimulated geothermal power plant. *Geothermics*, 52, 36-49.

Moriya, H., Niitsuma, H., & Baria, R. (2003). Multiplet-clustering analysis reveals structural details within the seismic cloud at the Soultz geothermal field, France. *Bulletin of the Seismological Society of America*, *93*(4), 1606-1620.

Mousavi, S. M., Ogwari, P. O., Horton, S. P., & Langston, C. A. (2017). Spatio-temporal evolution of frequency-magnitude distribution and seismogenic index during initiation of induced seismicity at Guy-Greenbrier, Arkansas. *Physics of the Earth and Planetary Interiors*, *267*, 53-66.

Mukuhira, Y., Asanuma, H., Niitsuma, H., & Häring, M. O. (2013). Characteristics of large-magnitude microseismic events recorded during and after stimulation of a geothermal reservoir at Basel, Switzerland. *Geothermics*, *45*, 1-17.

Mukuhira, Y., Dinske, C., Asanuma, H., Ito, T., & Häring, M. O. (2017). Pore pressure behavior at the shut‐in phase and causality of large induced seismicity at Basel, Switzerland. *Journal of Geophysical Research: Solid Earth*, *122*(1), 411-435.

Norbeck, J. H., & Rubinstein, J. L. (2018). Hydromechanical earthquake nucleation model forecasts onset, peak, and falling rates of induced seismicity in Oklahoma and Kansas. *Geophysical Research Letters*, *45*(7), 2963-2975.

Nur, A., & Byerlee, J. (1971). An exact effective stress law for elastic deformation of rock with fluids. *Journal of geophysical research*, *76*(26), 6414-6419.

Okubo, P. G., & Aki, K. (1987). Fractal geometry in the San Andreas fracture system. *Journal of Geophysical Research: Solid Earth*, *92*(B1), 345-355.

Postma, T., & Jansen, J. D. (2018). The Small Effect of Poroelastic Pressure Transients on Triggering of Production‐Induced Earthquakes in the Groningen Natural Gas Field. *Journal of Geophysical Research: Solid Earth*, *123*(1), 401-417.

Poupinet, G., Ellsworth, W. L., & Frechet, J. (1984). Monitoring velocity variations in the crust using earthquake doublets: An application to the Calaveras Fracture, California. *Journal of Geophysical Research: Solid Earth*, *89*(B7), 5719-5731.

Raziperchikolaee, S., Alvarado, V., & Yin, S. (2014). Microscale modeling of fluid flow‐geomechanics‐seismicity: Relationship between permeability and seismic source response in deformed rock joints. *Journal of Geophysical Research: Solid Earth*, 119(9), 6958-6975.

Rice, J. R., & Cleary, M. P. (1976). Some basic stress diffusion solutions for fluid‐saturated elastic porous media with compressible constituents. *Reviews of Geophysics*, *14*(2), 227-241.

Richards‐Dinger, K., & Dieterich, J. H. (2012). RSQSim earthquake simulator. *Seismological Research Letters*, *83*(6), 983-990.

Riffracture, J., Dempsey, D., Archer, R., Kelkar, S., & Karra, S. (2016). Understanding Poroelastic Stressing and Induced Seismicity with a Stochastic/Deterministic Model: an Application to an EGS Stimulation at Paralana, South Australia, 2011. *In Proc. 41st Stanford Workshop on Geothermal Reservoir Engineering*, SGP-TR-209.

Rothert, E., & Shapiro, S. A. (2007). Statistics of fracture strength and fluid‐induced microseismicity. *Journal of Geophysical Research: Solid Earth*, *112*(B4).

Rudnicki, J. W. (1986). Fluid mass sources and point forces in linear elastic diffusive solids. *Mechanics of Materials*, *5*(4), 383-393.

Schoenball, M., Davatzes, N. C., & Glen, J. M. (2015). Differentiating induced and natural seismicity using space‐time‐magnitude statistics applied to the Coso Geothermal field. *Geophysical Research Letters*, *42*(15), 6221-6228.

Scholz, C. H. (2015). On the stress dependence of the earthquake b value. *Geophysical Research Letters*, *42*(5), 1399-1402.

Scuderi, M. M., & Collettini, C. (2016). The role of fluid pressure in induced vs. triggered seismicity: Insights from rock deformation experiments on carbonates. *Scientific Reports*, *6*, 24852.

Segall, P. (1985). Stress and subsidence resulting from subsurface fluid withdrawal in the epicentral region of the 1983 Coalinga earthquake. *Journal of Geophysical Research: Solid Earth*, 90(B8), 6801-6816.

Segall, P. (1989). Earthquakes triggered by fluid extraction. *Geology*, *17*(10), 942-946.

Segall, P. (2010). *Earthquake and volcano deformation*. NJ: Princeton University Press.

Segall, P., & Fitzgerald, S. D. (1998). A note on induced stress changes in hydrocarbon and geothermal reservoirs. *Tectonophysics*, 289(1), 117-128.

Segall, P., & Lu, S. (2015). Injection ‐ induced seismicity: Poroelastic and earthquake nucleation effects. *Journal of Geophysical Research: Solid Earth*, *120*(7), 5082-5103.

Segall, P., Grasso, J. R., & Mossop, A. (1994). Poroelastic stressing and induced seismicity near the Lacq gas field, southwestern France. *Journal of Geophysical Research: Solid Earth*, *99*(B8), 15423-15438.

Shapiro, S. A., Dinske, C., Langenbruch, C., & Wenzel, F. (2010). Seismogenic index and magnitude probability of earthquakes induced during reservoir fluid stimulations. *The Leading Edge*, *29*(3), 304-309.

Shapiro, S. A., Huenges, E., & Borm, G. (1997). Estimating the crust permeability from fluid ‐ injection ‐ induced seismic emission at the KTB site. *Geophysical Journal International*, *131*(2).

Shapiro, S. A., Rentsch, S., & Rothert, E. (2005). Characterization of hydraulic properties of rocks using probability of fluid-induced microearthquakes. *Geophysics*, *70*(2), F27-F33.

Shapiro, S. A., Rothert, E., Rath, V., & Rindschwentner, J. (2002). Characterization of fluid transport properties of reservoirs using induced microseismicity. *Geophysics*, *67*(1), 212-220.

Shi, Y., & Bolt, B. A. (1982). The standard error of the magnitude-frequency b value. *Bulletin of the Seismological Society of America*, *72*(5), 1677-1687.

Skoumal, R. J., Ries, R., Brudzinski, M. R., Barbour, A. J., & Currie, B. S. (2018). Earthquakes induced by hydraulic fracturing are pervasive in Oklahoma. *Journal of Geophysical Research: Solid Earth*, *123*(12), 10-918.

Stabile, T. A., Giocoli, A., Perrone, A., Piscitelli, S., & Lapenna, V. (2014). Fluid injection induced seismicity reveals a NE dipping fracture in the southeastern sector of the High Agri Valley (southern Italy). *Geophysical Research Letters*, *41*(16), 5847-5854.

Stark, M. A., & Davis, S. D. (1996). Remotely triggered microearthquakes at The Geysers geothermal field, California. *Geophysical research letters*, 23(9), 945-948.

Stormo, A., Lengliné, O., & Schmittbuhl, J. (2015). Mechanical origin of b-value changes during stimulation of deep geothermal reservoirs. *Geothermal Energy*, *3*(1), 1.

Tafti, T. A., Sahimi, M., Aminzadeh, F., & Sammis, C. G. (2013). Use of microseismicity for determining the structure of the fracture network of large-scale porous media. *Physical Review E*, *87*(3), 032152.

Tarrahi, M., & Jafarpour, B. (2012). Inference of permeability distribution from injection ‐ induced discrete microseismic events with kernel density estimation and ensemble Kalman filter. *Water Resources Research*, *48*(10).

Terakawa, T. (2014). Evolution of pore fluid pressures in a stimulated geothermal reservoir inferred from earthquake focal mechanisms. *Geophysical Research Letters*, *41*(21), 7468-7476.

Terakawa, T., Miller, S. A., & Deichmann, N. (2012). High fluid pressure and triggered earthquakes in the enhanced geothermal system in Basel, Switzerland. *Journal of Geophysical Research: Solid Earth*, *117*(B7).

Terzaghi, Karl (1936). Relation Between Soil Mechanics and Foundation Engineering: Presidential Address. *Proceedings, First International Conference on Soil Mechanics and Foundation Engineering, Boston*. 3, 13-18.

Tung, S., & Masterlark, T. (2018). Delayed poroelastic triggering of the 2016 October Visso earthquake by the August Amatrice earthquake, Italy. *Geophysical Research Letters*, *45*(5), 2221-2229.

Tutuncu, A. N., & Bui, B. T. (2015). Coupled geomechanical and fluid flow modeling for injection induced seismicity prediction. In *SEG Technical Program Expanded Abstracts 2015* (pp. 4848-4852). Society of Exploration Geophysicists.

Van Wees, J. D., Buijze, L., Van Thienen-Visser, K., Nepveu, M., Wassing, B. B. T., Orlic, B., & Fokker, P. A. (2014). Geomechanics response and induced seismicity during gas field depletion in the Netherlands. *Geothermics*, *52*, 206-219.

Verdon, J. P., Stork, A. L., Bissell, R. C., Bond, C. E., & Werner, M. J. (2015). Simulation of seismic events induced by CO2 injection at In Salah, Algeria. *Earth and Planetary Science Letters*, *426*, 118-129.

Vermylen, J., & Zoback, M. D. (2011, January). Hydraulic fracturing, microseismic magnitudes, and stress evolution in the Barnett Shale, Texas, USA. In *SPE Hydraulic Fracturing Technology Conference*. Society of Petroleum Engineers.

Vujević, K., Graf, T., Simmons, C. T., & Werner, A. D. (2014). Impact of fracture network geometry on free convective flow patterns. *Advances in Water Resources*, 71, 65-80.

Waldhauser, F., & Ellsworth, W. L. (2002). Fracture structure and mechanics of the Hayward fracture, California, from double‐difference earthquake locations. *Journal of Geophysical Research: Solid Earth*, *107*(B3).

Wang, R., & Kümpel, H. J. (2003). Poroelasticity: Efficient modeling of strongly coupled, slow deformation processes in a multilayered half-space. *Geophysics*, *68*(2), 705-717.

Wangen, M. (2019). A 3D model of hydraulic fracturing and microseismicity in anisotropic stress fields. *Geomechanics and Geophysics for Geo-Energy and Geo-Resources*, *5*(1), 17-35.

Wassing, B. B. T., Van Wees, J. D., & Fokker, P. A. (2014). Coupled continuum modeling of fracture reactivation and induced seismicity during enhanced geothermal operations. *Geothermics*, 52, 153-164.

Watanabe, K., & Takahashi, H. (1995). Fractal geometry characterization of geothermal reservoir fracture networks. *Journal of Geophysical Research: Solid Earth*, *100*(B1), 521-528.

White, J. A., & Borja, R. I. (2011). Block-preconditioned Newton–Krylov solvers for fully coupled flow and geomechanics. *Computational Geosciences*, *15*(4), 647.

Yeck, W. L., Weingarten, M., Benz, H. M., McNamara, D. E., Bergman, E. A., Herrmann, R. B., ... & Earle, P. S. (2016). Far‐field pressurization likely caused one of the largest injection induced earthquakes by reactivating a large preexisting basement fracture structure. *Geophysical Research Letters*, *43*(19).

Yoon, J. S., Zang, A., & Stephansson, O. (2014). Numerical investigation on optimized stimulation of intact and naturally fractured deep geothermal reservoirs using hydro-mechanical coupled discrete particles joints model. *Geothermics*, 52, 165-184.

Yu, H., Harrington, R. M., Liu, Y., & Wang, B. (2019). Induced Seismicity Driven by Fluid Diffusion Revealed by a Near‐Field Hydraulic Stimulation Monitoring Array in the Montney Basin, British Columbia. *Journal of Geophysical Research: Solid Earth*, *124*(5), 4694-4709.

Zaliapin, I., & Ben‐Zion, Y. (2016). Discriminating characteristics of tectonic and human‐induced seismicity. *Bulletin of the Seismological Society of America*, *106*(3), 846-859.

Zbinden, D., Rinaldi, A. P., Urpi, L., & Wiemer, S. (2017). On the physics‐based processes behind production‐induced seismicity in natural gas fields. *Journal of Geophysical Research: Solid Earth*, 122(5), 3792-3812.

Zhao, X., & Paul Young, R. (2011). Numerical modeling of seismicity induced by fluid injection in naturally fractured reservoirs. *Geophysics*, 76(6), WC167-WC180.

Zoback, M. D., & Zinke, J. C. (2002). Production-induced normal fractureing in the Valhall and Ekofisk oil fields. *In The Mechanism of Induced Seismicity* (pp. 403-420). Basel: Birkhäuser.

Figure Captions

Figure 1. Schematic illustration (not to scale) of the hydro-mechanical-seismological modeling of fluid-induced seismicity plotted in the fracture effective normal stress-shear stress space. Based on the peak and residual frictional strengths of a fracture, as are depicted by the red and green lines, the space is divided into two parts defining the initial stress regime for a triggered event and an induced event, respectively (to be elaborated in section 4.3.3). The blue and magenta dots are given as two examples, both located on a Mohr circle defined by $\boldsymbol{\sigma}'_{f0}$. For either type of event, the modeling consists two steps. The first step is to predict the fracture stress by compensating the fracture with $\boldsymbol{\sigma}'_{fp}$, which requires the pore pressure modeling for case 1, the fracture-pore pressure modeling for case 2 and the fracture-poro-mechanical modeling for case 3, the latter two resolving the *LSDF*. The outcome of this step is indicated by the green and red arrows. The second step, which does not vary among the three cases, is to stochastically model $\Delta\tau$ on source fracture as indicated by the dashed arrows to approximately account for the effect of $\boldsymbol{\sigma}'_{fs}$; meanwhile, $\Delta\tau$ remains constrained on a range $\Delta\tau_{\max}$ as is indicated by the yellow arrows and it is computed from the poroelastic loading history $\boldsymbol{\sigma}'_{fp}$ in conjunction with $\boldsymbol{\sigma}'_{f0}$. Two consecutive seismic cycles *j* and *j+1* are shown, and the complete stress updating scheme is given in list 1.

Figure 2. (a) The model domain for cases 2 and 3. It consists of a *LSDF* embedded within an otherwise porous matrix. The color suggests the index *I* (see equation (21)). For case 1, the *LSDF* is removed from the domain. (b) Conforming space discretization of the fractured domain and the resulting unstructured triangular finite elements used in arriving at the semi-discrete forms. For case 3, all elements represent the porous hosting rock; the grey elements are the standard two-field (fluid pressure, solid displacement) mixed FE elements; the colored elements are 'hybrid' mixed elements in which at least one edge is also used as a lower-dimensional element to discretize the fractures; the color of an element indicates the I^{th} deterministic fracture with which it is associated. If a hybrid element conforms to multiple fractures, only the largest *I* is used for coloring. For case 2, the elements have similar meanings as in case 3 except they are no longer mixed (i.e., only used for interpolating the fluid pressure). For case 1, all elements are the standard single-field elements. Adapted from Jin & Zoback (2017).

Figure 3. The dual fracture network (*DF*, equation (42)) consisting of 12800 fractures used for the seismicity modeling, shown together with its two subsets A and B. (a)-(c) Cases 2 and 3, and (d)-(f) case 1. In case 1, fractures are essentially explicit visualizations of seismicity seeds assigned with random critical pore pressure values. Figures 3a shows the subset A with deterministic fracture locations and orientations as an approximation to the *LSDF* shown in figure 2a; figure 3b shows the subset B as a stochastic realization of fractures in the hosting rock; figure 3c shows the hybrid deterministic-stochastic *DF* in which the fracture length distribution follows a realistic power-law scaling relation. Figures 3d-3f resemble figures 3a-3c except for the stochastic fracture orientation in figure 3d. In all figures, the warm

color indicates the fracture is favorably oriented with respect to $\boldsymbol{\sigma}'_{f0}$ whereas the cool color indicates otherwise.

Figure 4. The initial stress used for the seismological modeling. In figure 4a, the initial effective normal stress and shear stress on all fractures (figures 3c, 3f) are plotted. Because the fractures sample all likely orientations, a Mohr circle is formed. The color indicates CFF_0. The peak and the residual strengths are also shown for reference (same as those in figure 1). The geometric meaning of CFF_0 is shown for one fracture as an example. Figures 4b, 4c show the histograms of CFF_0 for case 1 and cases 2-3, respectively.

Figure 5. Snapshots of the spatial distribution of the modeled quantities at four time steps for case 1. (a)-(d) The fluid overpressure δp_p and (e)-(f) the seismicity sized with M_w and colored with $\Delta\tau$. Only the 100 m × 100 m area around the center is shown. The time is indicated at the top of each plot.

Figure 6. Same as figure 5, but for case 2. The *LSDF* is shown in the background.

Figure 7. Snapshots of the spatial distribution of the modeled quantities at four time steps for case 3. (a)-(d) The fluid overpressure δp_p, (e)-(h) the first poroelastic stress invariant $I_1'/3$, (i)-(l) the second deviatoric poroelastic stress invariant $\sqrt{J_2'}$, (m)-(p) the excess poroelastic shear stress invariant $MC=\sqrt{J_2'}-sin(\phi)I_1'/3$ and (q)-(t) the seismicity sized with M_w and colored with $\Delta\tau$. Only the 100 m × 100 m area around the center is shown. The time is indicated at the top of each plot. The *LSDF* is shown in the background.

Figure 8. Space-time plots of the fluid overpressure δp_p. (a) Case 1, (b) case 2 and (c) case 3. The distance is only plotted from 0 to 45 m. The color scale is the same as in figures 5-7. Several characteristic diffusion profiles are shown (see text) as references, including the green and magenta lines calculated using the diffussivity of the hosting rock and the fractures, respectively. The differnces between cases 1 and 2 show the effect of the *LSDF* and the differences between cases 2 and 3 show the effect of poroelastic coupling.

Figure 9. Space-time plots of the poroelastic stress invariants for case 3. (a) $I_1'/3$, (b) $\sqrt{J_2'}$ and (c) $MC=\sqrt{J_2'}-sin(\phi)I_1'/3$. The distance is only plotted from 0 to 45 m and the characteristic diffusion profiles are the same as those in figure 13. The color scale is the same as figure 8. The counterparts of the three quantities in case 2 without the coupling effect can be obtained by multiplying the δp_p in figure 8b with -0.67, 0 and 0.34 (appendix A.1).

Figure 10. Space-time plots of all seismic events, sized with M_w and colored with CFF_0. (a), (d) Case 1, (b), (e) case 2 and (c), (f) case 3. The distance is only plotted from 0 to 45 m and the reference characteristic diffusion profiles are the same as those in figure 13. The differnces between cases 1 and 2

show the effect of the *LSDF* and the differences between cases 2 and 3 show the effect of poroelastic coupling.

Figure 11. Evolution of near-field events versus remotely triggered events in the fully coupled case 3. (a) - (h) Snapshots of the distribution of remotely triggered events (blue dots) overlaying areas undergoing poroelastic stressing (magnitude shown by the color) and negligible pressure changes, together with near-field events (magenta dots) overlaying areas (non-colored) where pore pressure changes are present. (i) The population of remote events (blue) relative to that of near-field events (magenta) plotted against time. Over time, the predominant triggering style transitions from near-field triggering to remote triggering. (j) *R-T* plot of the remote stress superposed with seismicity. The colored domain indicates possible space-time for remote triggering whereas non-colored domain indicates space-time for near-field triggering. Near-field events dominates at smaller distances and earlier time while remote events take over at greater distance and later time.

Figure 12. Repeating events sized with M_w and colored with t_0. (a) Case 1, (b) case 2 and (c) case 3. Only the 100 m × 100 m area around the center is shown. The number of groups and the total number of events are indicated at the top left. The *LSDF* in the background for cases 2 and 3.

Figure 13. Representative complete stress paths. (a) Case 1, (b) case 2 and (c) case 3. The color indicates the time. The number of seismic cycles is 6 in cases 1 and 2 and 3 in case 3. The pore pressure effect and the poroelastic effect are indicated.

Figure 14. Characteristics of the repeating events. (a)-(b) Case 1, (c)-(d) case 2 and (e)-(f) case 3. Figures 14a, 14c and 14e show the location of each group containing repeating events, colored with the number of events within that group (i.e., the number of seismic cycles the associated fracture has undergone). Figures 14b, 14d and 14f are histograms showing the distribution of the inter-event time between two consecutive repeating events.

Figure 15. Poisson's distribution of the inter-event time between consecutive repeating events and the associated parameters.

Figure 16. Triggered and induced events sized with M_w and colored with t_0. (a)-(b) Case 1, (c)-(d) case 2 and (e)-(f) case 3. Only the 100 m × 100 m area around the center is shown. The number of events is indicated at the top left. The *LSDF* is shown in the background.

Figure 17. The top row shows relationships among M_w, L and $\Delta\tau$ of all modeled events. Overlaying are four contours corresponding to $\Delta\tau$=0.01 MPa, 0.1 MPa, 1 MPa and 10 MPa. The bottom row shows the histograms of $\Delta\tau$ together with the cumulative frequency using 1000 equal-sized bins on the range [0.01, 10] MPa. Additionally, the number of events with $\Delta\tau \leq 0.01$ MPa, $0.01\text{MPa} < \Delta\tau \leq 0.1$ MPa, $0.1\text{MPa} < \Delta\tau \leq 1$

MPa and $\Delta\tau$>1 MPa are counted and the percentages are shown. (a), (b) Case 1, (c), (d) case 2 and (e), (f) case 3.

Figure 18. Histogram of fracture lengths using 1000 equal-sized bins, plotted on a log-log scale as discrete sequences. The green sequence indicates the distribution of lengths of all fractures, which follows a power law decay as is fitted with the magenta line. The fitting parameters are also shown, specifically, the fractal dimension D is 1. The red sequence shows the length distribution of activated fractures only (fractures undergone at least one seismic cycle). Because it is primarily the favorably oriented fractures that are activated, the distribution no longer follows a power law decay. (a) Case 1, (b) case 2 and (c) case 3.

Figure 19. Histogram of the modeled M_w (yellow green). The bin size is 0.05, and the y-axis is on a log-scale. The associated distribution of N follows the classic Gutenberg-Richter law (blue green); data points with a M_w above -2 are used for fitting (the magenta line), yielding a b-value around 2, which is commonly observed for induced micro-seismicity. (a) Case 1, (b) case 2 and (c) case 3.

Figure 1.

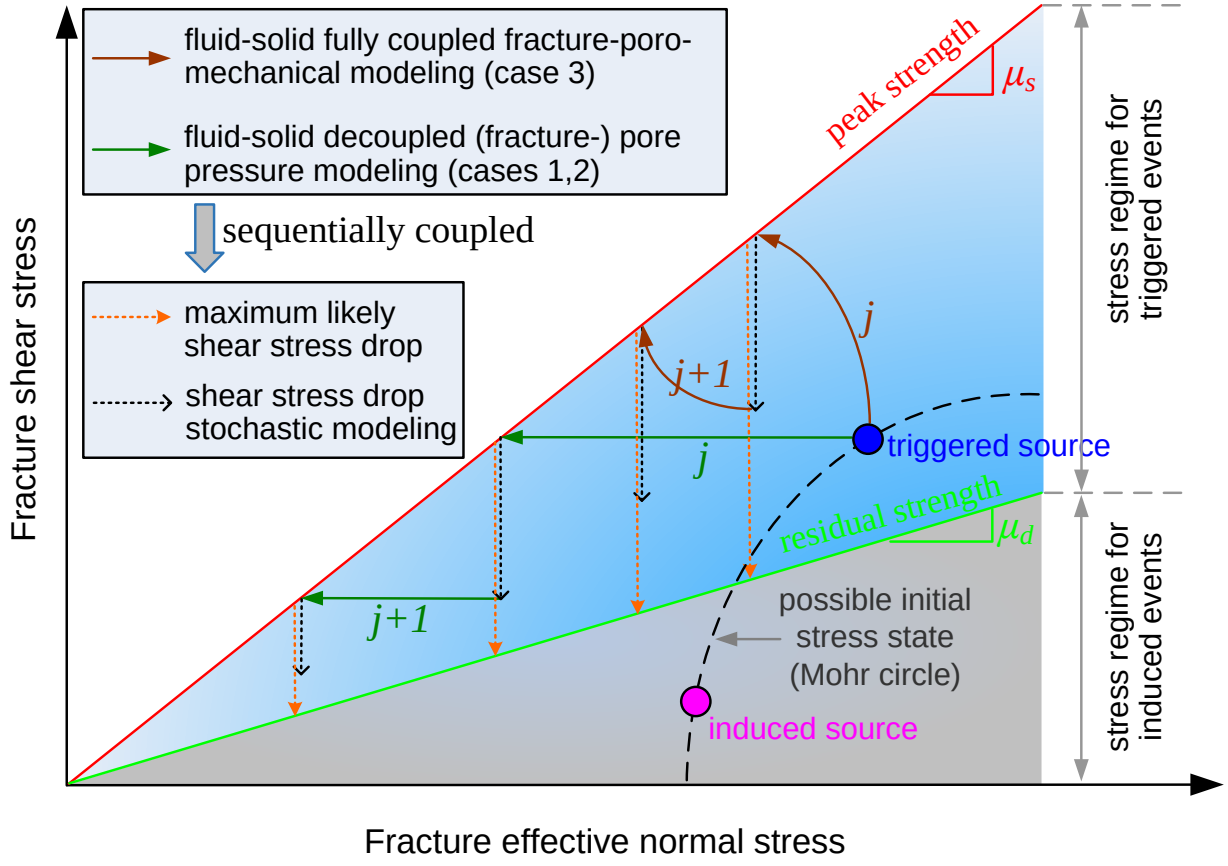
fluid-solid fully coupled fracture-poro-mechanical modeling (case 3)
fluid-solid decoupled (fracture-) pore pressure modeling (cases 1,2)
sequentially coupled
maximum likely shear stress drop
shear stress drop stochastic modeling
peak strength
μ_s
residual strength
μ_d
j
$j+1$
j
$j+1$
triggered source
possible initial stress state (Mohr circle)
induced source
stress regime for triggered events
stress regime for induced events
Fracture shear stress
Fracture effective normal stress

Figure 2.

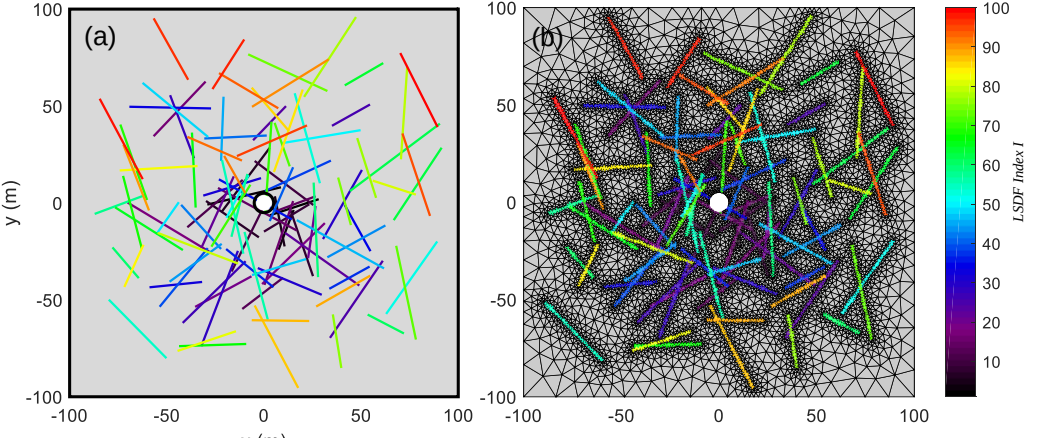
(a)
(b)
y (m)
x (m)
100
50
0
-50
-100
-100
-50
0
50
100
LSDF Index I
100
90
80
70
60
50
40
30
20
10

Figure 3.

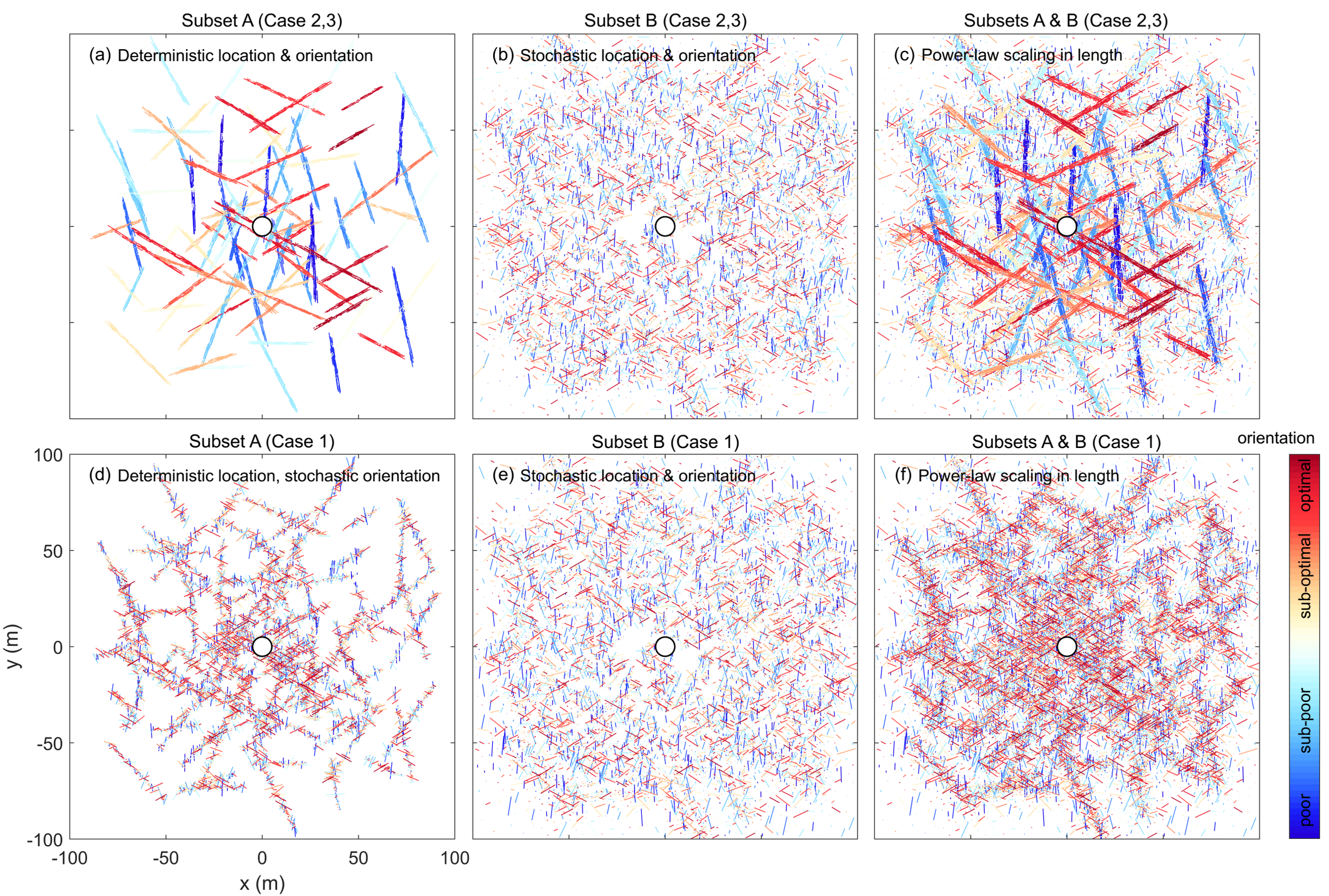
Subset A (Case 2,3)
Subset B (Case 2,3)
Subsets A & B (Case 2,3)
(a) Deterministic location & orientation
(b) Stochastic location & orientation
(c) Power-law scaling in length
Subset A (Case 1)
Subset B (Case 1)
Subsets A & B (Case 1)
(d) Deterministic location, stochastic orientation
(e) Stochastic location & orientation
(f) Power-law scaling in length
orientation
optimal
sub-optimal
sub-poor
poor
y (m)
x (m)
100
50
0
-50
-100
-100
-50
0
50
100

Figure 4.

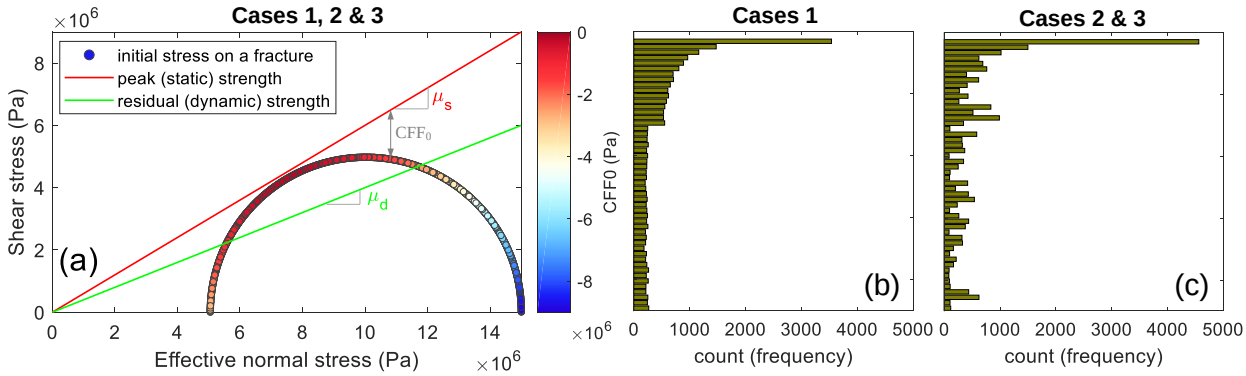
Cases 1, 2 & 3
×10^6
initial stress on a fracture
peak (static) strength
residual (dynamic) strength
μs
CFF0
μd
(a)
Shear stress (Pa)
Effective normal stress (Pa)
×10^6
CFF0 (Pa)
Cases 1
(b)
count (frequency)
Cases 2 & 3
(c)
count (frequency)

Figure 5.

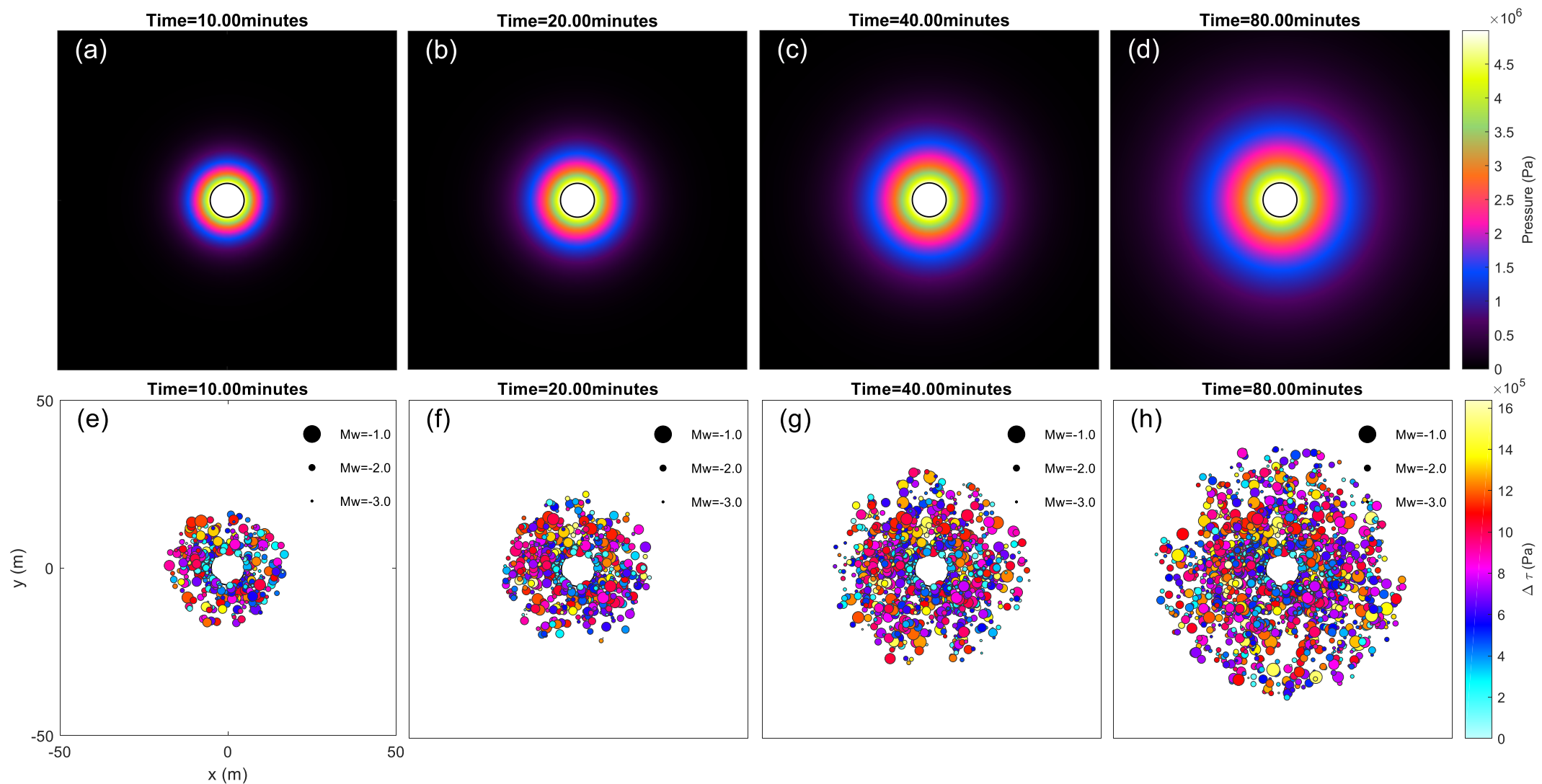
Time=10.00minutes
Time=20.00minutes
Time=40.00minutes
Time=80.00minutes
(a)
(b)
(c)
(d)
×10^6
4.5
4
3.5
3
2.5
2
1.5
1
0.5
0
Pressure (Pa)
Time=10.00minutes
Time=20.00minutes
Time=40.00minutes
Time=80.00minutes
(e)
(f)
(g)
(h)
Mw=-1.0
Mw=-2.0
Mw=-3.0
50
0
-50
y (m)
-50
0
50
x (m)
×10^5
16
14
12
10
8
6
4
2
0
Δ τ (Pa)

Figure 6.

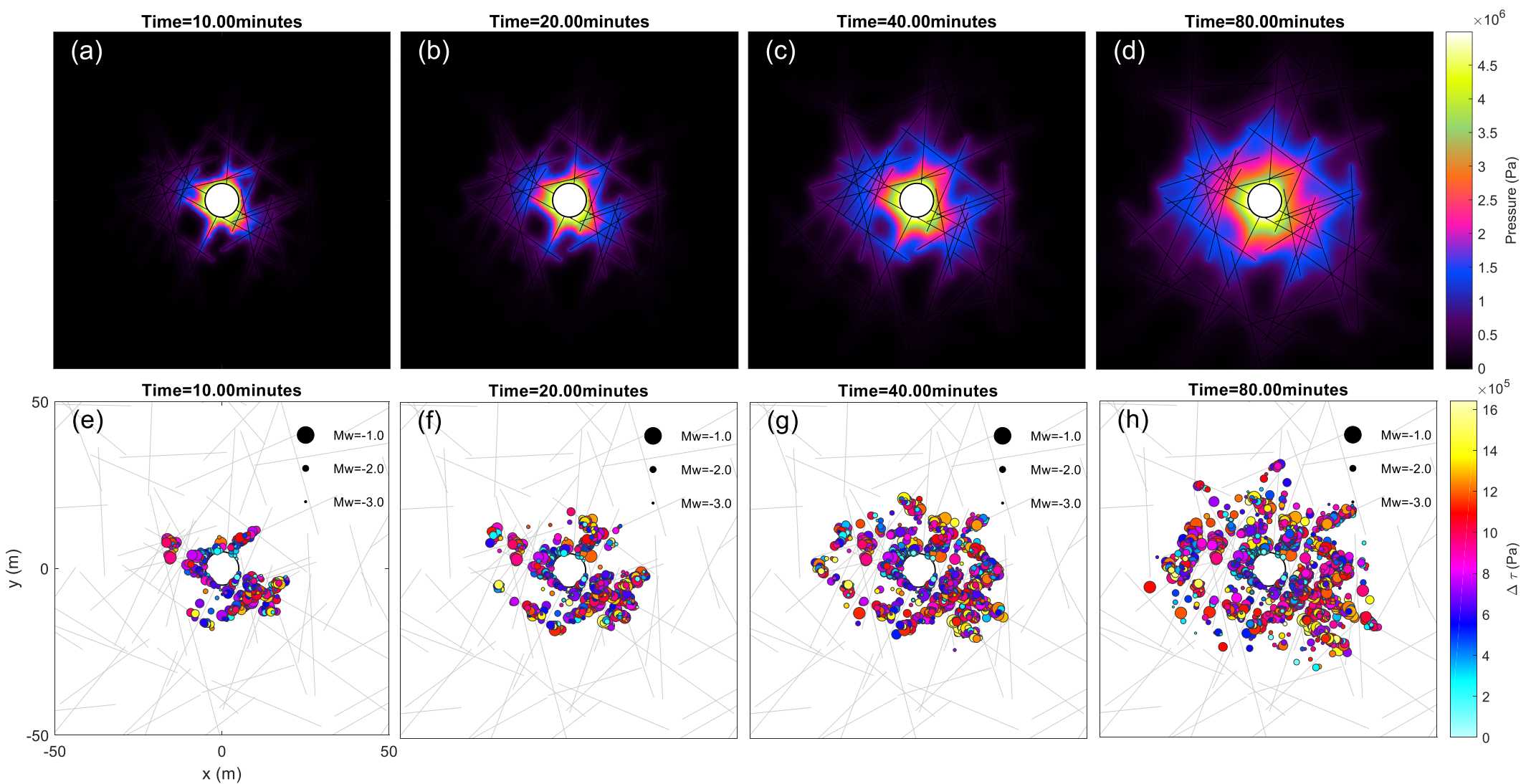
Time=10.00minutes
Time=20.00minutes
Time=40.00minutes
Time=80.00minutes
(a)
(b)
(c)
(d)
×10^6
4.5
4
3.5
3
2.5
2
1.5
1
0.5
0
Pressure (Pa)
Time=10.00minutes
Time=20.00minutes
Time=40.00minutes
Time=80.00minutes
(e)
(f)
(g)
(h)
Mw=-1.0
Mw=-2.0
Mw=-3.0
50
0
-50
y (m)
-50
0
50
x (m)
×10^5
16
14
12
10
8
6
4
2
0
Δ τ (Pa)

Figure 7.

Time=10.00minutes
Time=20.00minutes
Time=40.00minutes
Time=80.00minutes
(a)
(b)
(c)
(d)
×10^6
4.5
4
3.5
3
2.5
2
1.5
1
0.5
0
Pressure (Pa)
Time=10.00minutes
Time=20.00minutes
Time=40.00minutes
Time=80.00minutes
(e)
(f)
(g)
(h)
×10^6
0
-0.2
-0.4
-0.6
-0.8
-1
-1.2
-1.4
-1.6
-1.8
-2
1/3*I1'(Pa)
Time=10.00minutes
Time=20.00minutes
Time=40.00minutes
Time=80.00minutes
(i)
(j)
(k)
(l)
×10^5
5
4.5
4
3.5
3
2.5
2
1.5
1
0.5
√ J2'(Pa)
Time=10.00minutes
Time=20.00minutes
Time=40.00minutes
Time=80.00minutes
(m)
(n)
(o)
(p)
×10^5
16
14
12
10
8
6
4
2
0
√ J2'-sin(ϕ)*1/3*I1'(Pa)
Time=10.00minutes
Time=20.00minutes
Time=40.00minutes
Time=80.00minutes
(q)
(r)
(s)
(t)
Mw=-1.0
Mw=-2.0
Mw=-3.0
50
0
-50
y (m)
-50
0
50
x (m)
×10^5
16
14
12
10
8
6
4
2
0
Δ τ (Pa)

Figure 8.

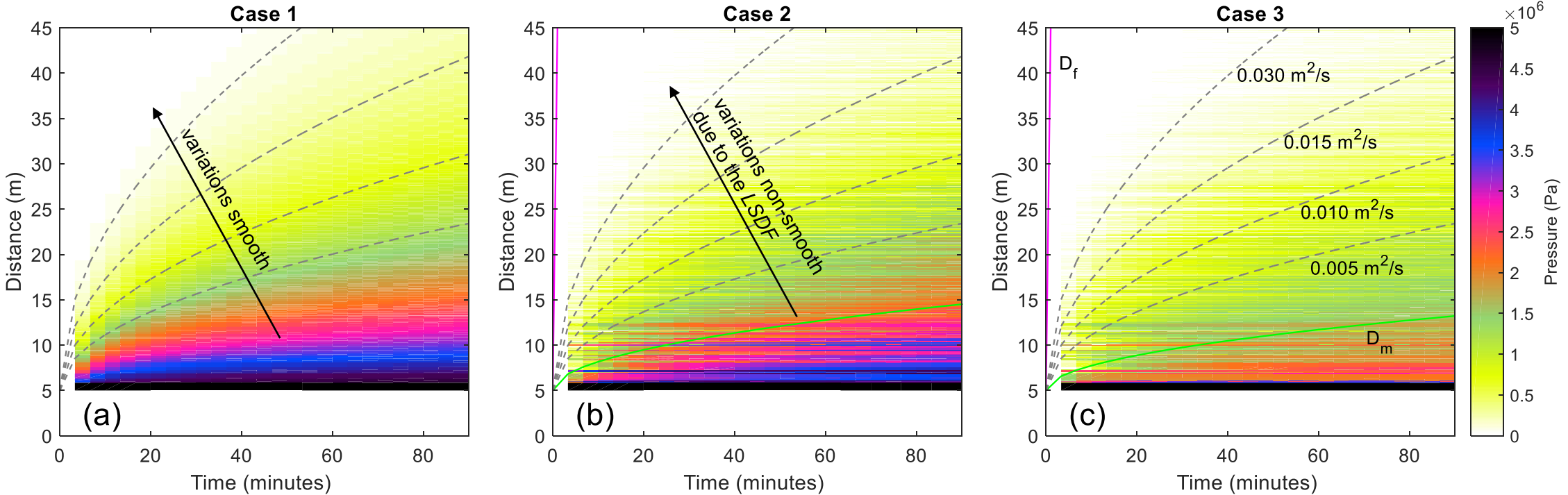
Case 1
Case 2
Case 3
Distance (m)
Time (minutes)
Pressure (Pa)
×10^6
variations smooth
variations non-smooth due to the LSDF
D_f
D_m
0.030 m^2/s
0.015 m^2/s
0.010 m^2/s
0.005 m^2/s
(a)
(b)
(c)

Figure 9.

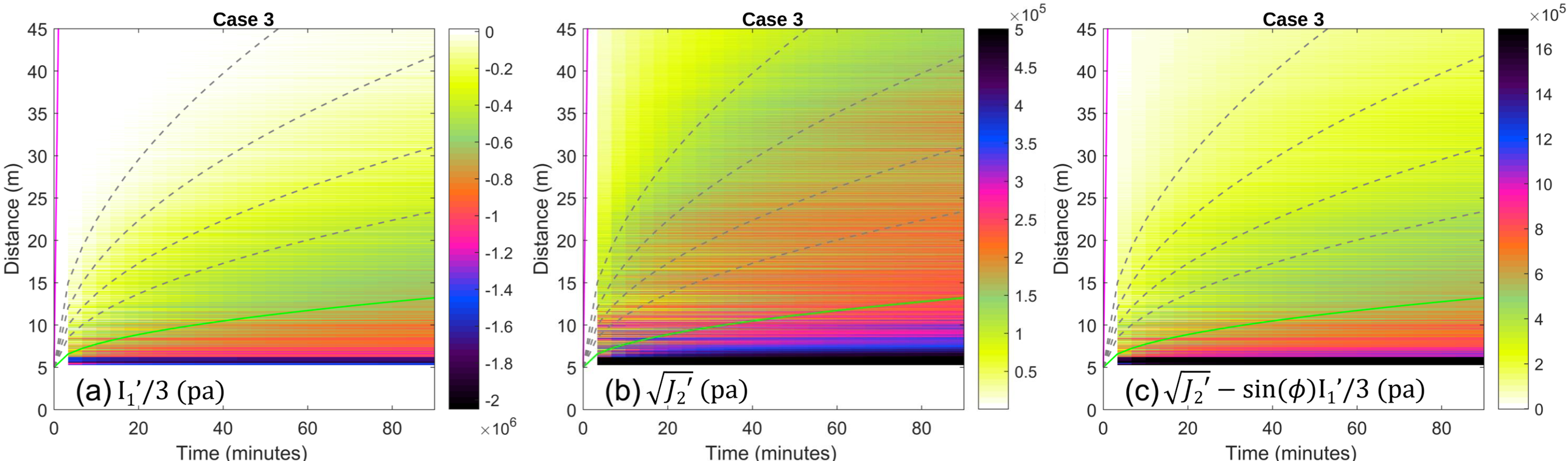
Case 3
Distance (m)
Time (minutes)
(a) $I_1'/3$ (pa)
$\times 10^6$
Case 3
Distance (m)
Time (minutes)
(b) $\sqrt{J_2'}$ (pa)
$\times 10^5$
Case 3
Distance (m)
Time (minutes)
(c) $\sqrt{J_2'} - \sin(\phi) I_1'/3$ (pa)
$\times 10^5$

Figure 10.

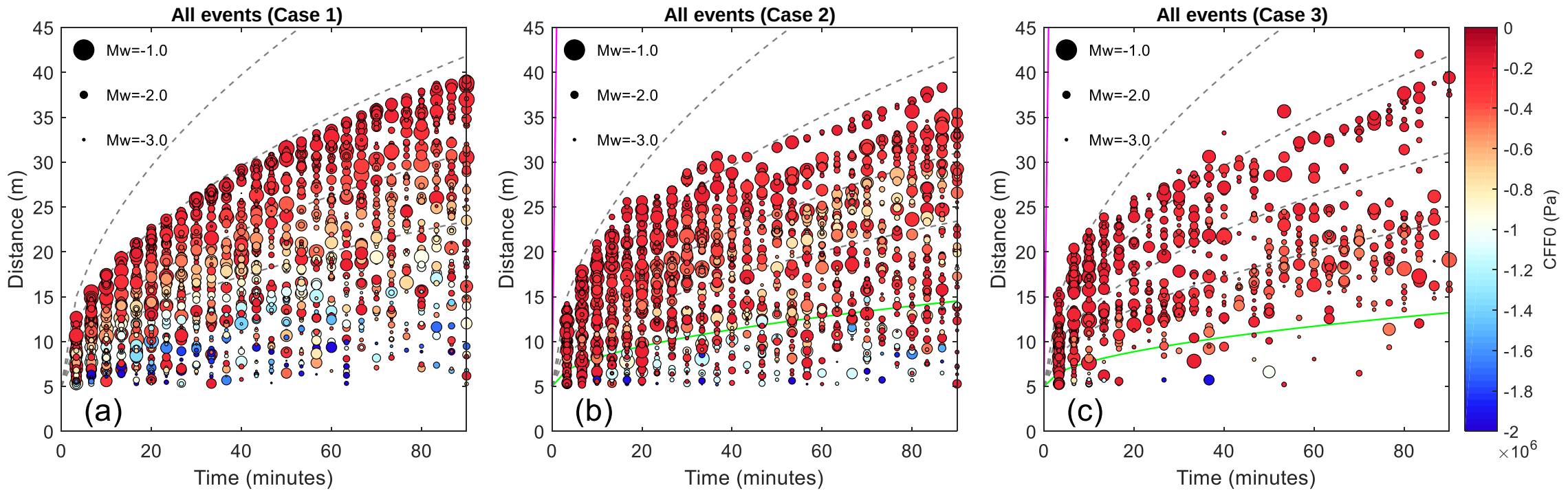
All events (Case 1)
All events (Case 2)
All events (Case 3)
Mw=-1.0
Mw=-2.0
Mw=-3.0
Distance (m)
Time (minutes)
(a)
(b)
(c)
CFF0 (Pa)
×10^6

Figure 11.

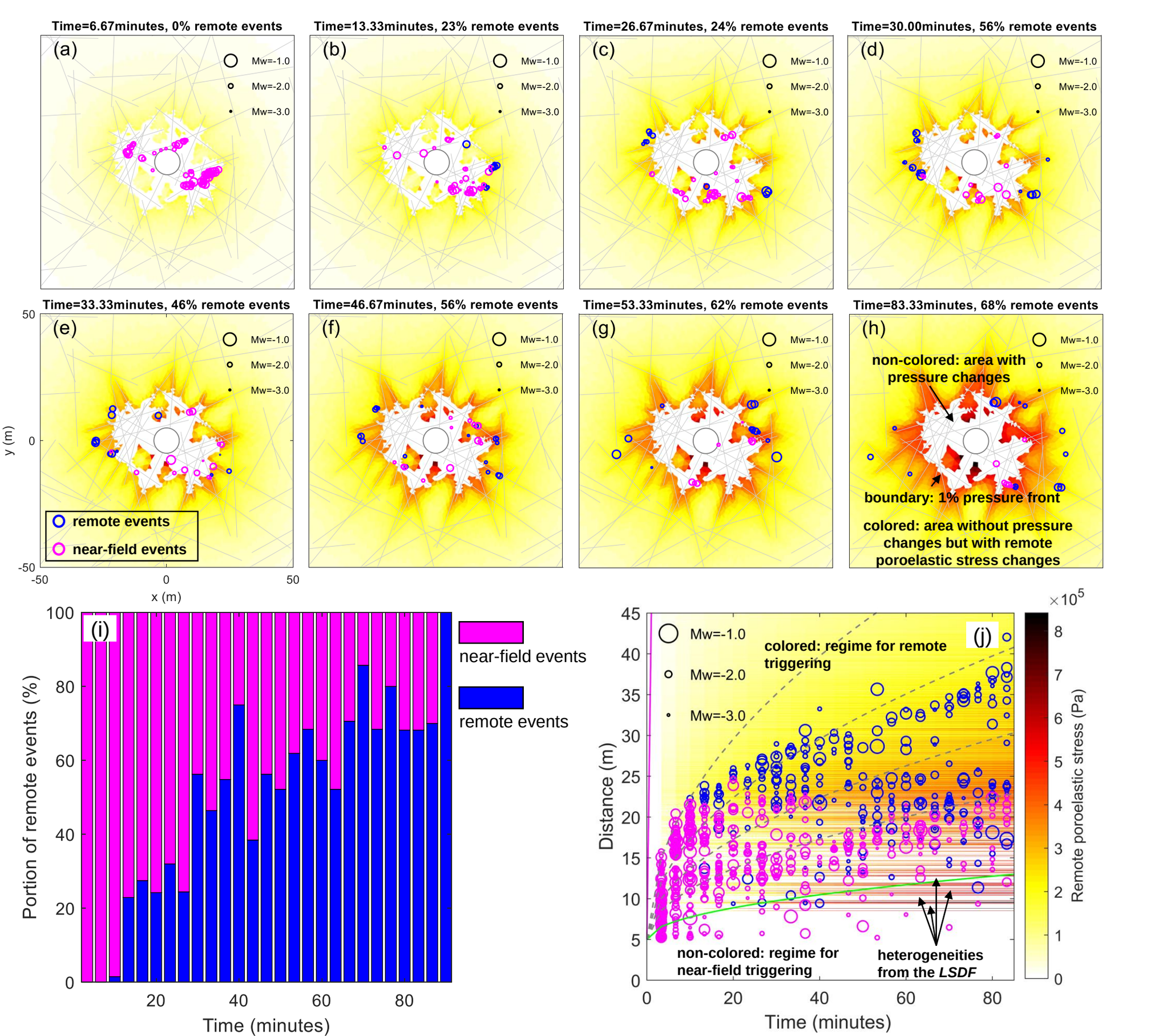
Time=6.67minutes, 0% remote events
Time=13.33minutes, 23% remote events
Time=26.67minutes, 24% remote events
Time=30.00minutes, 56% remote events
Time=33.33minutes, 46% remote events
Time=46.67minutes, 56% remote events
Time=53.33minutes, 62% remote events
Time=83.33minutes, 68% remote events
(a)
(b)
(c)
(d)
(e)
(f)
(g)
(h)
Mw=-1.0
Mw=-2.0
Mw=-3.0
remote events
near-field events
non-colored: area with pressure changes
boundary: 1% pressure front
colored: area without pressure changes but with remote poroelastic stress changes
x (m)
y (m)
(i)
near-field events
remote events
Portion of remote events (%)
Time (minutes)
(j)
colored: regime for remote triggering
non-colored: regime for near-field triggering
heterogeneities from the LSDF
Distance (m)
Time (minutes)
Remote poroelastic stress (Pa)

Figure 12.

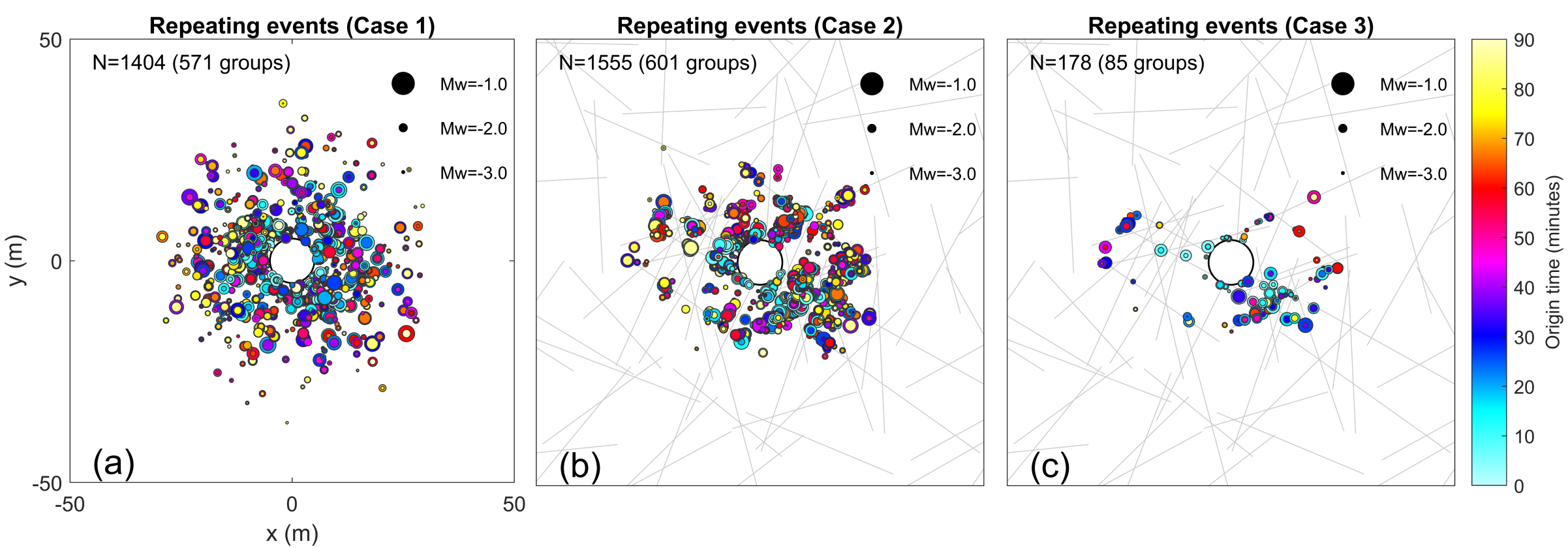
Repeating events (Case 1)
N=1404 (571 groups)
Mw=-1.0
Mw=-2.0
Mw=-3.0
(a)
Repeating events (Case 2)
N=1555 (601 groups)
Mw=-1.0
Mw=-2.0
Mw=-3.0
(b)
Repeating events (Case 3)
N=178 (85 groups)
Mw=-1.0
Mw=-2.0
Mw=-3.0
(c)
y (m)
x (m)
50
0
-50
-50
0
50
Origin time (minutes)
90
80
70
60
50
40
30
20
10
0

Figure 13.

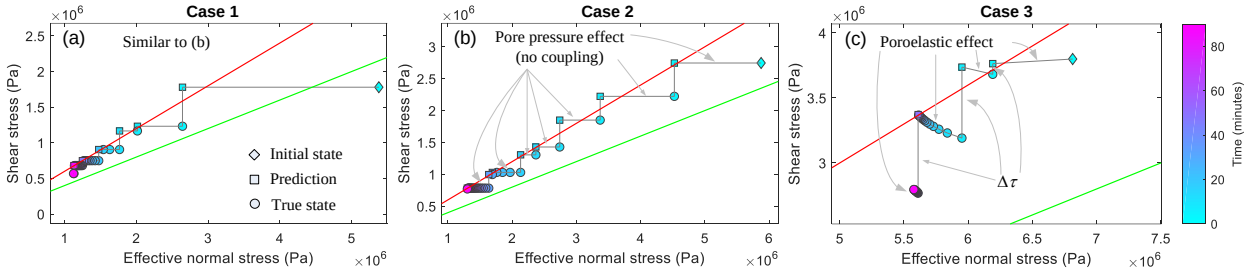
Case 1
(a)
Similar to (b)
Initial state
Prediction
True state
Shear stress (Pa)
Effective normal stress (Pa)
Case 2
(b)
Pore pressure effect
(no coupling)
Shear stress (Pa)
Effective normal stress (Pa)
Case 3
(c)
Poroelastic effect
$\Delta\tau$
Shear stress (Pa)
Effective normal stress (Pa)
Time (minutes)

Figure 14.

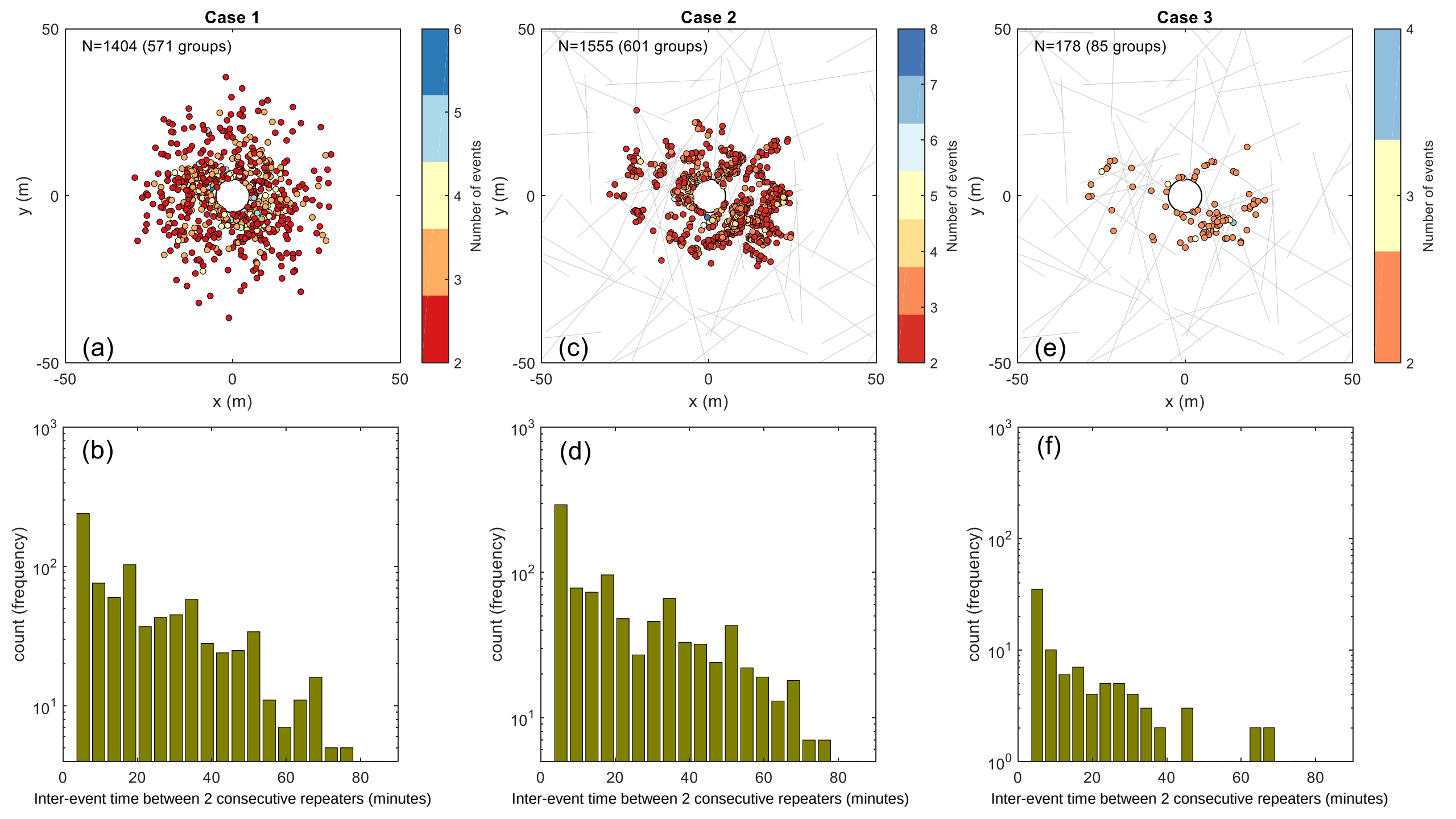
Case 1
N=1404 (571 groups)
(a)
y (m)
x (m)
Number of events
Case 2
N=1555 (601 groups)
(c)
Case 3
N=178 (85 groups)
(e)
(b)
(d)
(f)
count (frequency)
Inter-event time between 2 consecutive repeaters (minutes)

Figure 15.

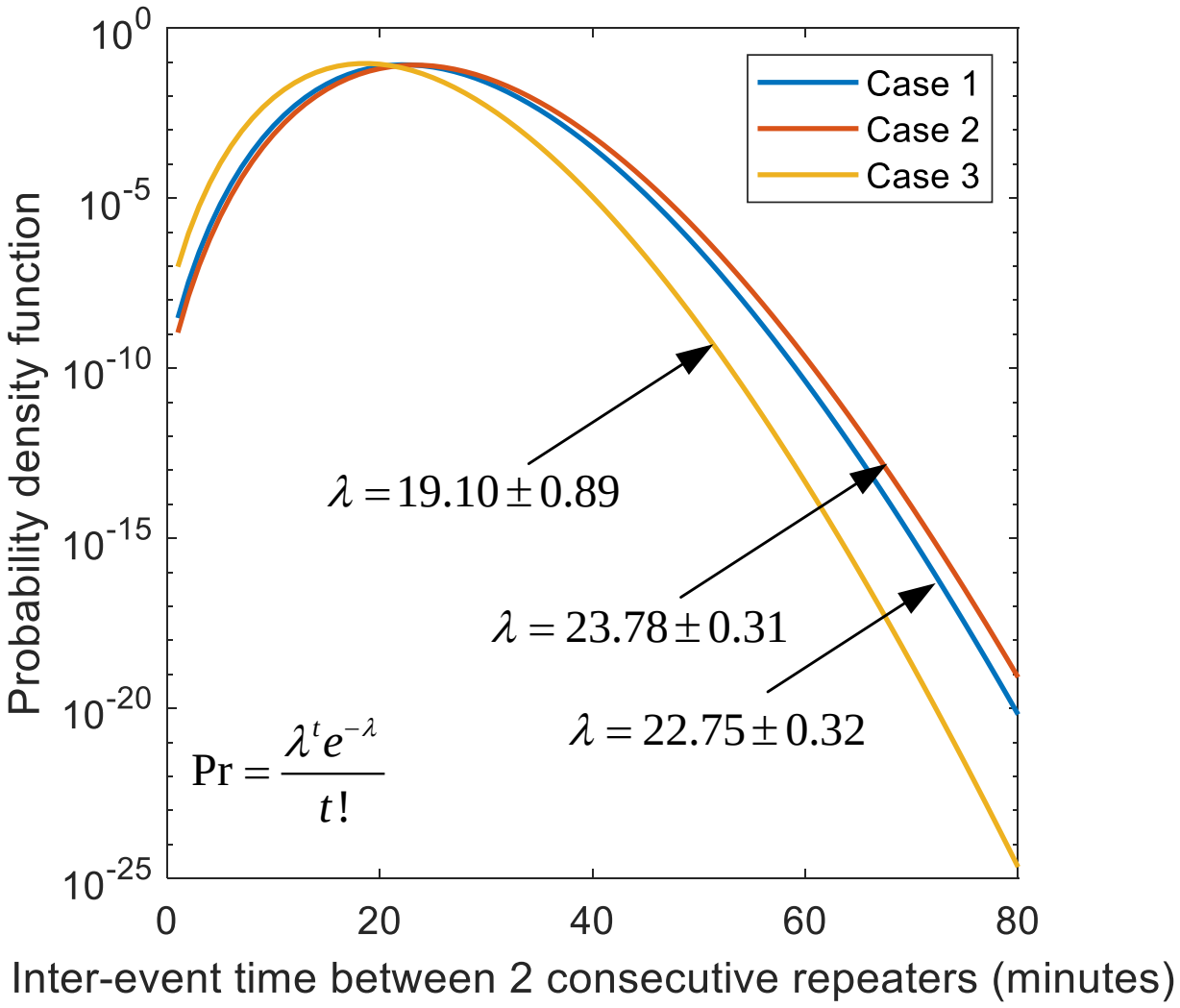
Probability density function
Inter-event time between 2 consecutive repeaters (minutes)
Case 1
Case 2
Case 3
$\lambda = 19.10 \pm 0.89$
$\lambda = 23.78 \pm 0.31$
$\lambda = 22.75 \pm 0.32$
$\Pr = \frac{\lambda^t e^{-\lambda}}{t!}$
10^0
10^{-5}
10^{-10}
10^{-15}
10^{-20}
10^{-25}
0
20
40
60
80

Figure 16.

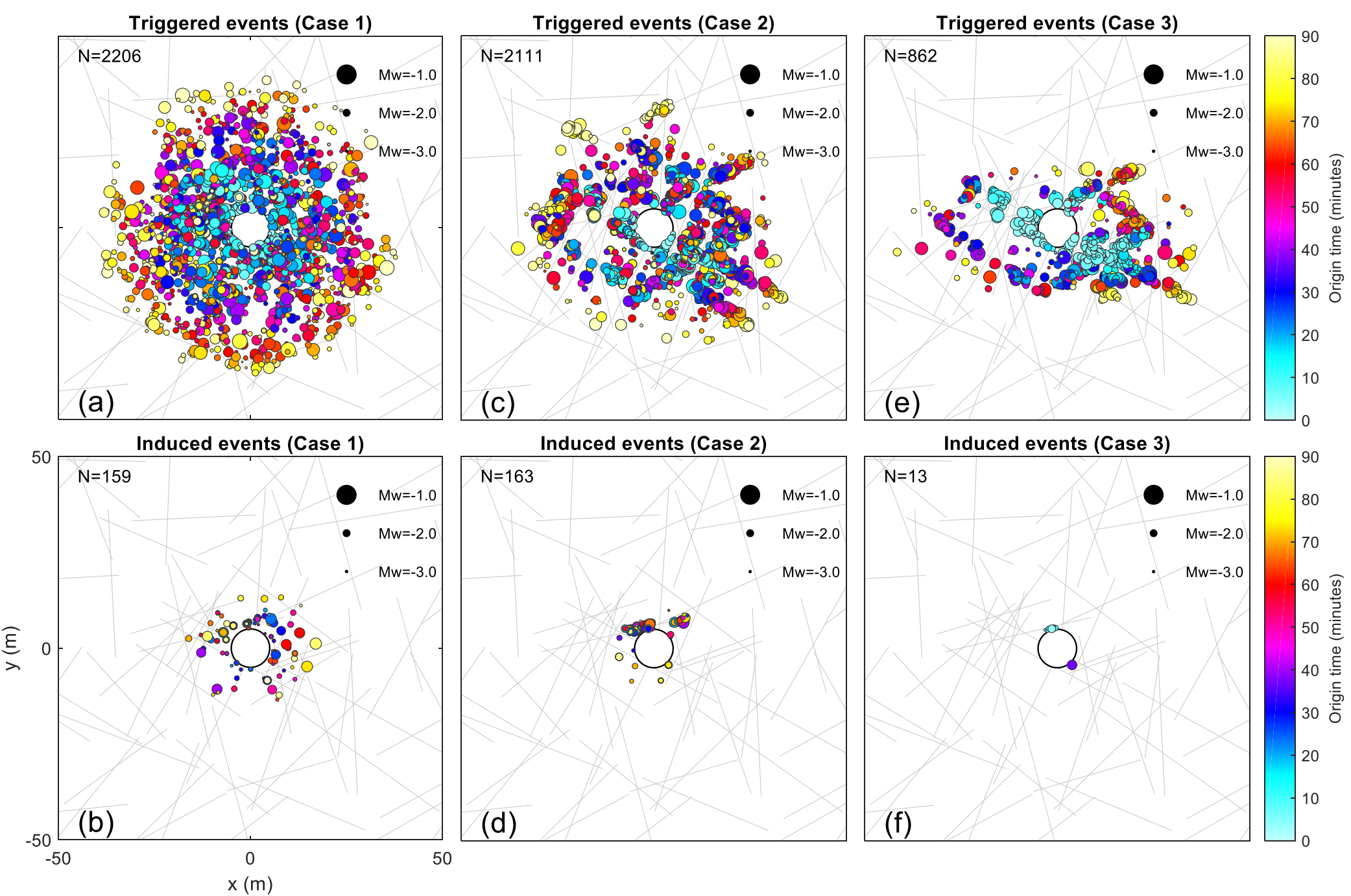
Triggered events (Case 1)
N=2206
Mw=-1.0
Mw=-2.0
Mw=-3.0
(a)
Triggered events (Case 2)
N=2111
Mw=-1.0
Mw=-2.0
Mw=-3.0
(c)
Triggered events (Case 3)
N=862
Mw=-1.0
Mw=-2.0
Mw=-3.0
(e)
Origin time (minutes)
0
10
20
30
40
50
60
70
80
90
Induced events (Case 1)
N=159
Mw=-1.0
Mw=-2.0
Mw=-3.0
(b)
Induced events (Case 2)
N=163
Mw=-1.0
Mw=-2.0
Mw=-3.0
(d)
Induced events (Case 3)
N=13
Mw=-1.0
Mw=-2.0
Mw=-3.0
(f)
y (m)
50
0
-50
x (m)
-50
0
50

Figure 17.

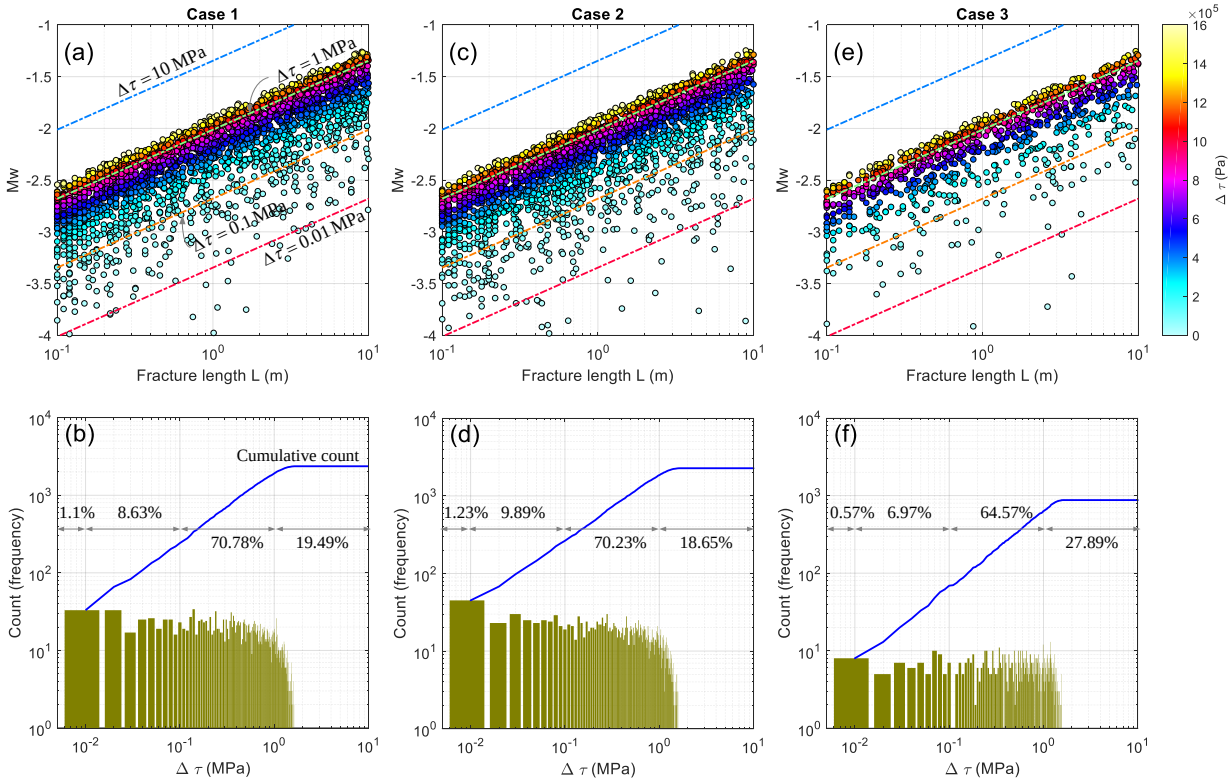
Case 1
Case 2
Case 3
(a)
(c)
(e)
(b)
(d)
(f)
Mw
Fracture length L (m)
Count (frequency)
Δ τ (MPa)
Δ τ (Pa)
×10^5
Δτ = 10 MPa
Δτ = 1 MPa
Δτ = 0.1 MPa
Δτ = 0.01 MPa
Cumulative count
1.1%
8.63%
70.78%
19.49%
1.23%
9.89%
70.23%
18.65%
0.57%
6.97%
64.57%
27.89%

Figure 18.

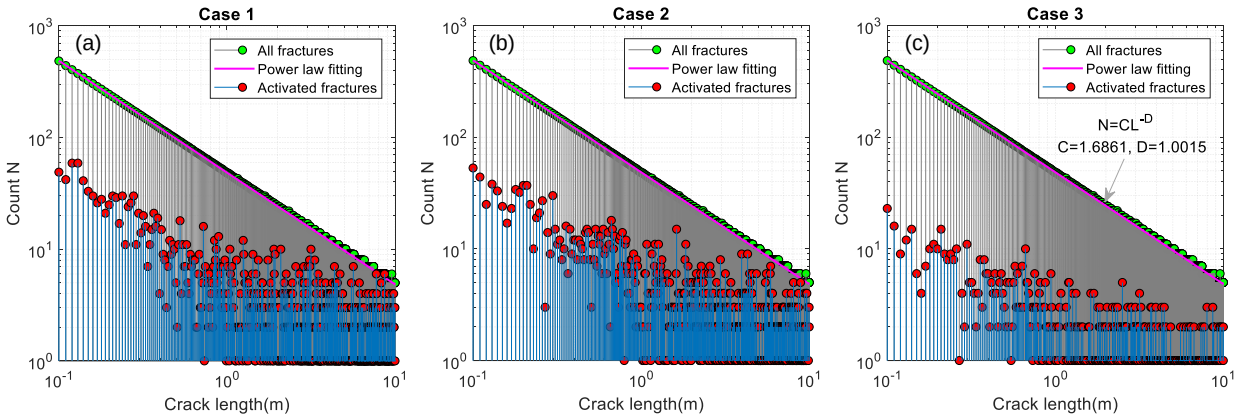
Case 1
(a)
All fractures
Power law fitting
Activated fractures
Count N
Crack length(m)
Case 2
(b)
All fractures
Power law fitting
Activated fractures
Count N
Crack length(m)
Case 3
(c)
All fractures
Power law fitting
Activated fractures
N=CL-D
C=1.6861, D=1.0015
Count N
Crack length(m)

Figure 19.

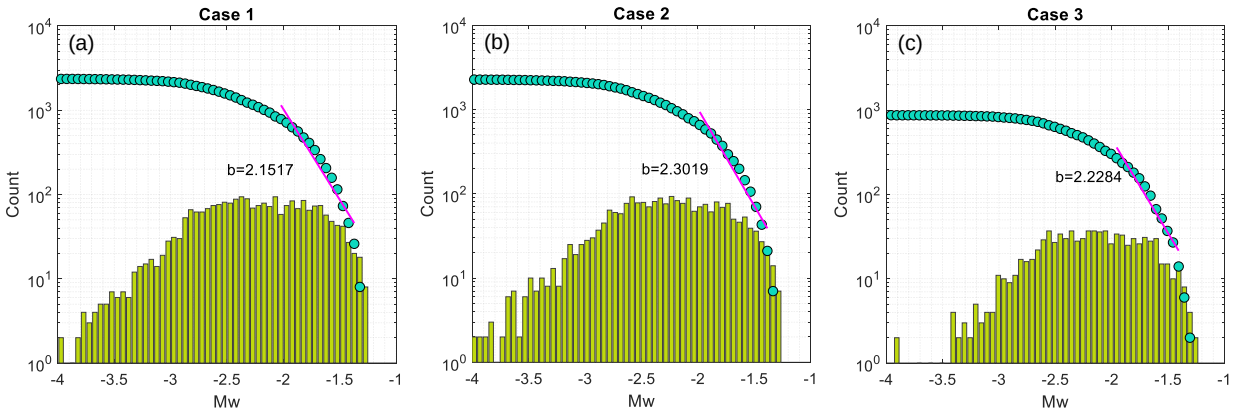
Case 1
(a)
b=2.1517
Count
Mw
Case 2
(b)
b=2.3019
Count
Mw
Case 3
(c)
b=2.2284
Count
Mw